HAL
open science

Denudation intensity and control in the Chinese Tian Shan: new constraints from mass balance on catchment-alluvial fan systems

Laure Guerit, Laurie Barrier, Marc Jolivet, Bihong Fu, François Métivier

To cite this version:

Laure Guerit, Laurie Barrier, Marc Jolivet, Bihong Fu, François Métivier. Denudation intensity and control in the Chinese Tian Shan: new constraints from mass balance on catchment-alluvial fan systems. Earth Surface Processes and Landforms, 2016, 41 (8), pp.1088-1106. 10.1002/esp.3890 . insu-01249993

HAL Id: insu-01249993

https://insu.hal.science/insu-01249993v1

Submitted on 6 Nov 2020

HAL is a multi-disciplinary open access archive for the deposit and dissemination of scientific research documents, whether they are published or not. The documents may come from teaching and research institutions in France or abroad, or from public or private research centers.

L'archive ouverte pluridisciplinaire **HAL**, est destinée au dépôt et à la diffusion de documents scientifiques de niveau recherche, publiés ou non, émanant des établissements d'enseignement et de recherche français ou étrangers, des laboratoires publics ou privés.

EARTH SURFACE PROCESSES AND LANDFORMS
Earth Surf. Process. Landforms (2016)
Copyright © 2016 John Wiley & Sons, Ltd.
Published online in Wiley Online Library
(wileyonlinelibrary.com) DOI: 10.1002/esp.3890

Denudation intensity and control in the Chinese Tian Shan: new constraints from mass balance on catchment-alluvial fan systems

Laure Guerit,[1,2]* Laurie Barrier,[1] Marc Jolivet,[3] Bihong Fu[4] and François Métivier[1]
[1] Institut de Physique du Globe de Paris, Sorbonne Paris Cité, Université Paris Diderot, UMR 7154 CNRS, F-75005 Paris, France
[2] Department of Earth Science, University of Geneva, 1205 Geneva, Switzerland
[3] Université Rennes 1, Laboratoire Géosciences Rennes, UMR6118 CNRS/INSU, Campus de Beaulieu, 35042 Rennes, France
[4] State Key Laboratory of Lithospheric Evolution, Institute of Geology and Geophysics, Chinese Academy of Sciences, Beijing, China

Received 12 May 2015; Revised 26 November 2015; Accepted 7 December 2015

*Correspondence to: Laure Guerit, Department of Earth Science, University of Geneva, 1205 Geneva, Switzerland. E-mail: laure.guerit@unige.ch

ESPL
Earth Surface Processes and Landforms

ABSTRACT: Tectonics and climate are usually seen as the main controlling factors of denudation rates, which seem to rise with the tectonic activity and to decrease when the climate becomes drier. However, the low denudation rates observed in semi-arid to arid contexts are generally measured on orogenic plateaus where the respective influence of the flat relief and the dry climate cannot really be unravelled. The Chinese Tian Shan was chosen as a case study. In the northern piedmont of this mountain range, a series of well-preserved Quaternary alluvial fans offer the opportunity to perform a mass balance study at the scale of several catchment areas and several hundreds of thousands of years. Based on a geometrical reconstruction of these fans, the volumes of sediments exported out of 10 drainage basins during the Middle–Late Pleistocene (from ~300 to ~12 kyr) and the Holocene (from ~12 kyr to present) have been estimated. From these volumes, an average denudation rate of ~135 m/Myr was determined in the Tian Shan Range for the last 300 kyr. In agreement with other mass balances performed in the same area, the typical denudation intensity of the northern Tian Shan is thus of a few hundred meters per million years at most, regardless of the space and time scales considered. From a comparison with denudation rates in other mountain ranges throughout the world, we suggest that a dry climate can dramatically limit the denudation intensity even in active orogenic systems with a high topographic gradient like the Tian Shan. As a result, the time required to reach equilibrium between denudation and rock uplift in these systems could be extremely long (i.e. of more than several million years). Copyright © 2016 John Wiley & Sons, Ltd.

KEYWORDS: denudation; mass balance; alluvial fan; Tian Shan; climate

Introduction

Denudation is a key process for mountain range evolution and the quantification of denudation rates is crucial to better constrain topography dynamics and mass transfer in orogenic systems (e.g. Molnar and England, 1990; Métivier *et al.*, 1999; Kirchner *et al.*, 2001; Farías *et al.*, 2008; Simoes *et al.*, 2010), as well as interactions between erosion, tectonics and climate (e.g. Raymo and Ruddiman, 1992; Avouac and Burov, 1996; Whipple, 2009; Iaffaldano *et al.*, 2011).

These two forcings are usually seen as the main controlling factors of the denudation intensity (e.g. Riebe *et al.*, 2001; Zhang *et al.*, 2001; Vance *et al.*, 2003; Binnie *et al.*, 2010), but their respective influences depend strongly on the studied areas. Tectonics can be the dominant control (e.g. Riebe *et al.*, 2001; Burbank *et al.*, 2003; von Blanckenburg, 2005; Herman *et al.*, 2010) or climate (e.g. Reiners *et al.*, 2003; Grujic *et al.*, 2006; Clift *et al.*, 2008), and in some contexts it is not possible to determine the prevalence of one or the other (e.g. Dadson *et al.*, 2003; Clift, 2006). Nonetheless, two trends seem to emerge from the existing data compilations (Wittmann *et al.*, 2007; Matmon *et al.*, 2009; Covault *et al.*, 2013): denudation rate rises with the tectonic activity whereas it decreases when the climate becomes more arid.

However, studies in semi-arid to arid contexts mostly focused on orogenic plateaus, such as the Tibet or Andes interiors (e.g. Lal *et al.*, 2004; Chappell *et al.*, 2006; Kober *et al.*, 2007; Kong *et al.*, 2007; Hippe *et al.*, 2012). Yet low denudation rates could also be linked to flat relief (e.g. Summerfield and Hulton, 1994; Montgomery and Brandon, 2002; Carretier *et al.*, 2013), hence the climatic control cannot really be asserted on plateaus. Very few studies have quantified denudation in orogenic systems where precipitations are less than 500 mm/yr but with strong topographic gradient (Ali *et al.*, 2003; Pan *et al.*, 2010) and there is still a clear need to document denudation in such ranges.

Denudation rates are often determined by thermochronology (e.g. Bullen *et al.*, 2003; Dadson *et al.*, 2003; Grujic *et al.*, 2006; Jolivet *et al.*, 2007, 2013a), cosmogenic isotopes (e.g. Brown *et al.*, 1995; Granger *et al.*, 1996; von Blanckenburg, 2005; Charreau *et al.*, 2011), or mass balances (Hinderer, 2012, and references therein). The mass balance

studies usually consist of sediment budgets from sedimentary basins or of sediment load measurements in present-day rivers (e.g. Métivier and Gaudemer, 1997; Gabet *et al.*, 2008; Barnes and Heins, 2009; Liu *et al.*, 2011; Calvès *et al.*, 2013). These approaches face several issues. On one hand, sediment budgets from sedimentary basins provide long-term values averaged over large areas. On the other hand, sediment load measurements give short-term values specific to the sampling location. Unless there is evidences that measurements can be extended over the whole drainage basin, huge field sampling efforts are then necessary to have a general view of the sediment budget within a complete river system.

Occasionally, mass balance is also performed on catchment–fan systems (Kiefer *et al.*, 1997; Oguchi, 1997; Allen and Hovius, 1998; Jayko, 2005; Hornung *et al.*, 2010; Jolivet *et al.*, 2014). They cover intermediate scales that are complementary to those of other sediment budget approaches, both in space and time (Hinderer, 2012). In fact, catchment–fan mass balances offer a better spatial resolution than sediment budgets from sedimentary basins. They are also more integrative in space and time, and they are easier to implement than sediment load measurements. For these reasons, catchment–fan sediment budgets are of great interest in discussing the evolution of denudation in space and/or time in a given area. However, the characteristic denudation intensity in a region over different time scales can only be determined if all these methods are used together (e.g. Kirchner *et al.*, 2001; Dadson *et al.*, 2003; Matmon *et al.*, 2003).

The Chinese Tian Shan Range is a high mountain belt located in Central Asia (Figure 1a) in a semi-arid to arid climate and it was chosen as a case study. On its northern side, which rises from 600 m a.s.l. up to more than 5000 m a.s.l., denudation rates have already been estimated by several methods, at different space and time scales (Métivier and Gaudemer, 1997; Charreau *et al.*, 2011; Liu *et al.*, 2011; Puchol, 2013; Jolivet *et al.*, 2014). In this area, the piedmont is formed by a series of exceptionally well-preserved Quaternary alluvial fans (Avouac *et al.*, 1993; Poisson, 2002; Lu *et al.*, 2010). They are located at the transition between the catchment areas and the sedimentary foreland basin, which is a strategic position to record the denudation history of the range. Moreover, rivers have deeply incised the old fans, whose basal surfaces are presently visible in outcrop. These fans offer the opportunity to improve the existing denudation data of the mountain range by a mass balance at intermediate space and time scales (several drainage basins and several hundred of thousands years).

In this paper, the methodology and results of this mass balance are presented, before discussing the denudation intensity and controls in the northern Tian Shan. From a comparison with denudation rates in other ranges, we suggest that dry climatic conditions strongly limit the denudation magnitude even in ranges where the topographic gradient is high, notwithstanding the tectonics activity.

Geological Setting

The Tian Shan is an east–west, 2500 km long, and up to 7400 m high, mountain belt that extends over western China, Kazakhstan and Kyrgyzstan (Figure 1a). After a complex Palaeozoic and Mesozoic orogenic history (e.g. Windley *et al.*, 1990; Allen *et al.*, 1992; Hendrix *et al.*, 1992; Gao *et al.*, 1998; Zhou *et al.*, 2001; Jolivet *et al.*, 2010, 2013b), the Tian Shan was reactivated during the Cenozoic in response to the India–Asia collision (e.g. Tapponnier and Molnar, 1977; Avouac *et al.*, 1993; Hendrix *et al.*, 1994; Dumitru *et al.*, 2001; Charreau *et al.*, 2009a; Jolivet *et al.*, 2010). Today, the range is still active, with a mean GPS shortening rate of up to ~2 cm/yr (Abdrakhmatov *et al.*, 1996; Reigber *et al.*, 2001; Zubovich *et al.*, 2010). In its Chinese part, the northern side of the range is separated from the Junggar foreland basin by three series of east–west oriented fault propagation folds (Figure 1b). A major thrust zone generally separates this faulted and folded piedmont from the exhumed basement that forms the high range (Avouac *et al.*, 1993; Burchfiel *et al.*, 1999; Guan *et al.*, 2009; Lu *et al.*, 2010; Chen *et al.*, 2014). In the piedmont, the slope rarely exceeds 25°, but it rises up to 40° in the range (Figure 1c).

Over the whole Cenozoic, the regional climate oscillated between semi-humid and semi-arid periods (Molnar *et al.*, 1994; Rhodes *et al.*, 1996; Yi *et al.*, 2004; Poisson and Avouac, 2004; Gallaud, 2008; Sun and Zhang, 2008; Xu *et al.*, 2010), and for the last 550 kyr several phases of glacial advances have been recorded in relation to the global glacial–interglacial cycles (Zhao *et al.*, 2009). The last major deglaciation occurred about 12 kyr ago and was followed by a period of more abundant precipitations (Rhodes *et al.*, 1996; Poisson and Avouac, 2004). However, since 6 kyr, the region has become increasingly arid. Nowadays, the regional climate is continental and semi-arid, influenced by the Westerlies and the Asian monsoon. Precipitation is typically less than 250 mm/yr in the northern piedmont (from 250 mm/yr around the city of Urumqi to less than 100 m/yr in the West), and rises up to 300–400 mm/yr in the range (Métivier and Gaudemer, 1997; Poisson, 2002; Sobel *et al.*, 2003).

In China, a dozen large rivers drain the northern side of the range (Figure 1b). They originate from glaciers in the hinterland mountains at an elevation of ~4000 m a.s.l. and flow northwards to the Junggar Basin, located about 3300 m below. In the piedmont, these rivers have built and incised several alluvial fans (Avouac *et al.*, 1993; Poisson, 2002; Lu *et al.*, 2010) (Figure 2). At least three sequences of fan growth, followed by abandonment and incision (Figure 2), occurred over the last 550 kyr (Zhou *et al.*, 2002; Lu *et al.*, 2010). The last abandonment–fan growth sequence initiated about 12 kyr ago during the last deglaciation (Avouac *et al.*, 1993; Poisson, 2002; Poisson and Avouac, 2004; Lu *et al.*, 2010; Gong *et al.*, 2014). According to optically stimulated luminescence, electron spin resonance, ^{10}Be and ^{14}C dating, the alluvial fans abandoned at that time (called F3 in Lu *et al.* (2010) and F_p in this study, see Table I for term definitions) are Middle–Late Pleistocene in age, as they were active between ~300 kyr and ~12 kyr for a total period of 277 ± 30 kyr (Molnar *et al.*, 1994; Poisson, 2002; Poisson and Avouac, 2004; Lu *et al.*, 2010; Yang *et al.*, 2013; Gong *et al.*, 2014). These fans are now deeply incised by up to 300 m deep canyons carved by the rivers (the KMZ coordinates of the river paths are given in Supplementary Data SA – supporting information) during the Holocene. As a consequence, the F_p fan basal surface is sometimes visible along the cliffs surrounding active river channels (Figures 2b and 3). Contemporaneous with this incision, a new generation of fans formed downstream in the Junggar Basin. These fans (called F4 in (Lu *et al.*, 2010) and F_h in this study) are Holocene in age and have been active for a period of 11.3 ± 2.3 kyr (Poisson and Avouac, 2004; Lu *et al.*, 2010). Remains of older fans exist in the region (F1 and F2 in Lu *et al.*, 2010), but this study focuses on the two last generations only.

All the catchment–fan systems of the northern side of the Chinese Tian Shan exhibit similar and probably coeval fan systems and canyons, which developed during the last glacial and interglacial periods (Molnar *et al.*, 1994; Poisson, 2002; Poisson and Avouac, 2004; Lu *et al.*, 2010; Gong *et al.*,

Copyright © 2016 John Wiley & Sons, Ltd.

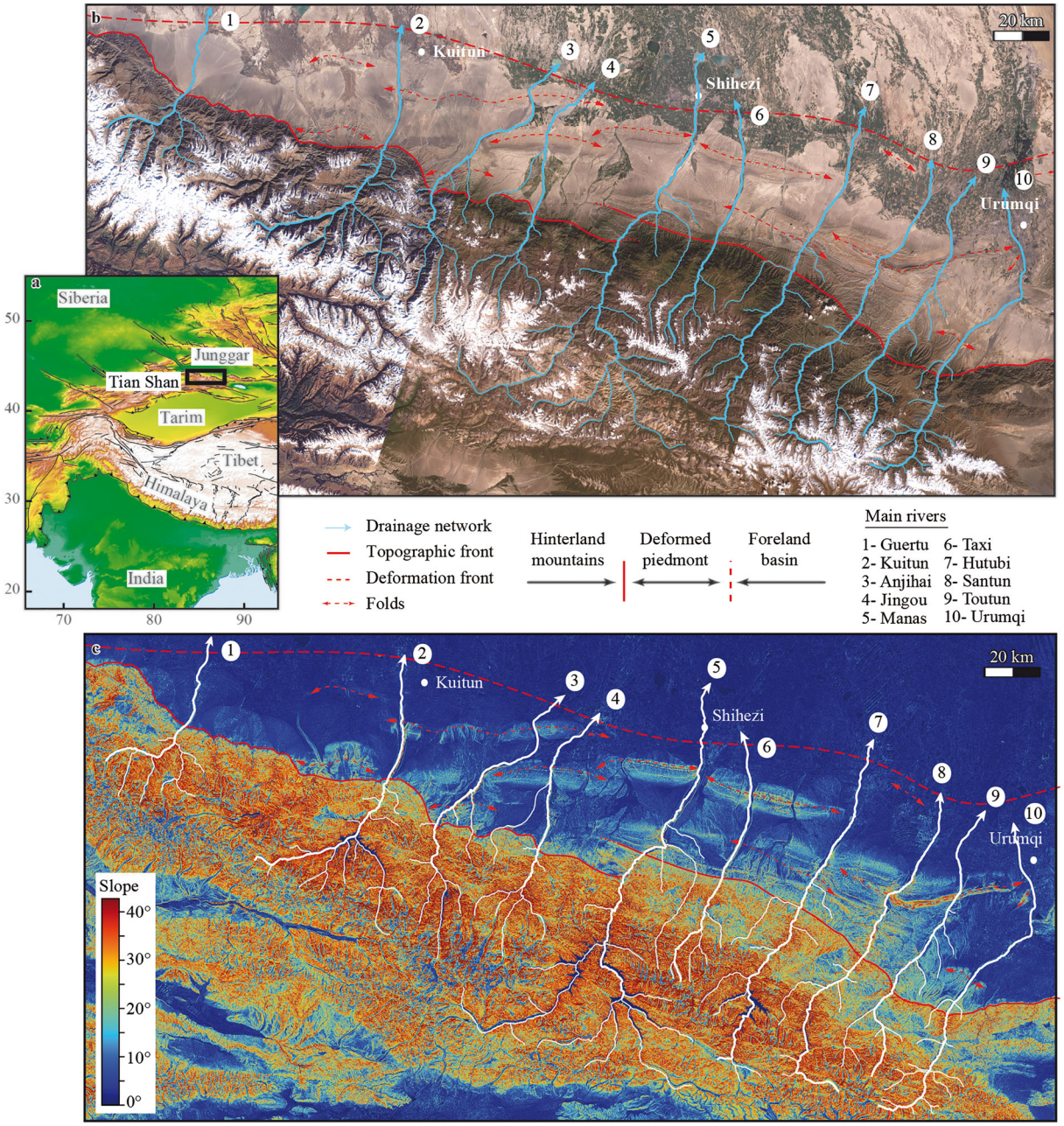

Figure 1. (a) Location of the Tian Shan; (b) satellite imagery (Landsat picture); (c) slope map of the northern side of the Chinese Tian Shan. The 10 river systems considered are named after Zhou *et al.* (1999). This figure is available in colour online at www.interscience.wiley.com/journal/espl.

2014). Moreover, the locations of the river incisions generally do not correlate with active tectonic structures. For example, along the ~40 km long Kuitun River canyon, tectonic uplift affects a zone of ≃5 km in length, which is known as the Dushanzi anticline. It has been shown by Poisson (2002) and Poisson and Avouac (2004) that this anticline cannot account for more than 10% of the local incision. Consequently, the fan aggradation–incision cycle is climate-driven and linked to changes in water and/or sediment discharges (Poisson, 2002; Poisson and Avouac, 2004).

Finally, the fans F_p and F_h are made up by conglomerates with grains from silts to metric boulders, with a porosity of 20 ± 10% (Clarke, 1979; Guerit, 2014). The Urumqi River is the only river where the sediment transport is quantitatively documented. Measurements in the upper part of its catchment show that 17.3 ± 0.3% of the material is transported as bedload, 35.2 ± 6.7% as suspended load and 47.5 ± 6.5% as dissolved load (Liu *et al.*, 2011). Based on the morphological similarities between the catchment–fan systems in northern Chinese Tian Shan, we assumed that these ratios are identical along the whole river path and through time, for all the studied systems.

Data and Methodology

The objective of this study was, first, to determine the volume of sediments that have been exported out of the drainage basins and deposited in the fans F_p and F_h, and secondly, to convert these volumes into denudation rates for the Middle–Late Pleistocene (from ~300 kyr to ~12 kyr) and the Holocene (from ~12 kyr to present).

In order to reconstruct the sediment volumes, two morpho-sedimentary maps of the northern side of the Chinese Tian Shan were drawn to locate accurately the Middle–Late Pleistocene and Holocene alluvial fans and their catchment areas based on satellite images (Landsat and Digital Globe

Copyright © 2016 John Wiley & Sons, Ltd.

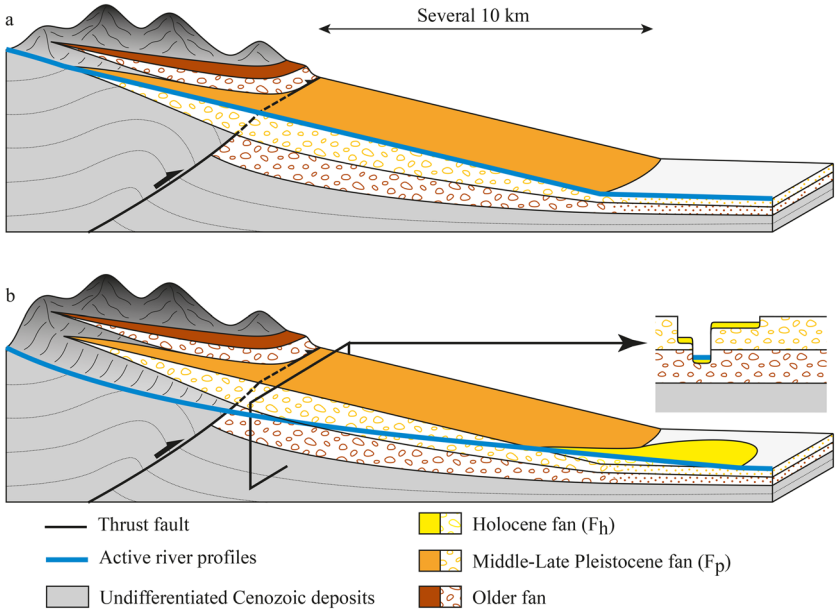

Figure 2. Morphology in cross-section of the northern Chinese Tian Shan piedmont (a) at the end of the Pleistocene and (b) nowadays, after the incision of the Middle–Late Pleistocene fans. The basal surface of these fans is now exposed along the cliffs surrounding active river channels. This figure is available in colour online at www.interscience.wiley.com/journal/espl.

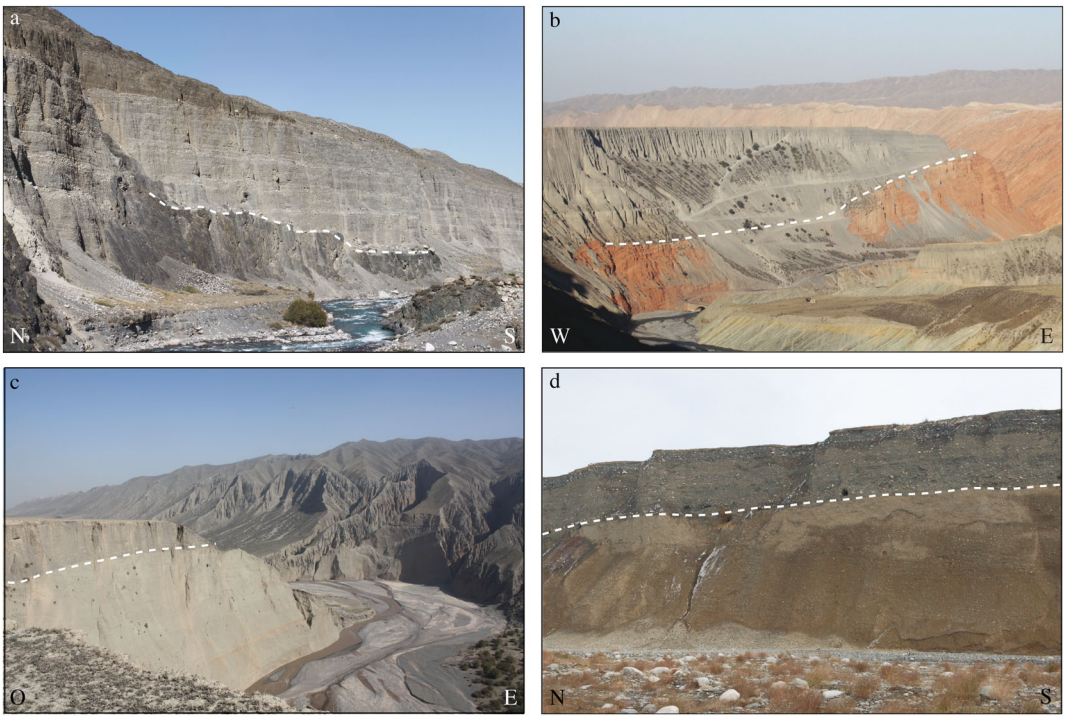

Figure 3. Outcrops of Middle–Late Pleistocene fan basal surfaces along the (a) Guertu, (b) Anjihai, (c) Hutubi and (d) Urumqi rivers. These basal surfaces (white dash lines) are emphasized by a contrast in (a, b, c, d) colour, and (a, b) lithology between the dark-grey deposits of the Pleistocene fans and the older terrains. In the presented examples, these terrains correspond to (a) Paleozoic bedrock, (b) Tertiary orange silts, sandstones and conglomerates, and (c, d) Tertiary and Quaternary light-grey conglomerates. The cliffs are a few dozen (d) up to a few hundred (b) metres high. This figure is available in colour online at www.interscience.wiley.com/journal/espl.

pictures) and a digital elevation model (ASTER GDEM2). The DEM were then used to model the fan top surfaces, and field data to reconstruct the fan basal surfaces. From these modelled surfaces, isopach maps were obtained and the volumes of sediments trapped in the fans were calculated. These volumes were converted into Middle–Late Pleistocene and Holocene denudation rates for each drainage basin, which were averaged to estimate the denudation rate of the whole northern side of the Tian Shan.

Morpho-sedimentary maps of the catchment–fan systems

Several morpho-sedimentary maps of the region are available, but the different data used and the variety of purposes have led to inconsistencies between these published documents (Avouac *et al.*, 1993; Poisson, 2002; Graveleau, 2008; Charreau *et al.*, 2009b; Lu *et al.*, 2010). In particular, the extension of fans and drainage basins differ from one map

Copyright © 2016 John Wiley & Sons, Ltd.

Table I. Terms and definitions used in this study

Term	Definition
F_p	Middle–Late Pleistocene fans
F_h	Holocene fan.
A_{F_p}	Areas of the fans F_p
A_{F_h}	Areas of the fans F_h
A_{dp}	Areas of the Middle–Late Pleistocene drainage basins
A_{dh}	Areas of the Holocene drainage basins
$A_{d,h-p}$	Areas of the Holocene extension of the drainage basins
V_{F_p}	Volumes of the fans F_p
V_{F_h}	Volumes of the fans F_h
V_c	Volumes of the Holocene canyons dug into the piedmont
$V_{\lambda F_p}$	Volumes of sediments in the fans F_p
$V_{\lambda F_h}$	Volumes of sediments in the fans F_h
$V_{\lambda c}$	Volumes of sediments removed from the Holocene canyons
V_{λ,F_h-c}	Difference between the volumes of sediments trapped in the fans F_h and removed from the Holocene canyons
λ	Sediment porosity (20 ± 10%)
α	Fraction of the total river load trapped in fans (17.3 ± 0.3%)
P_p	Period of F_p fan construction (277 ± 30 kyr)
P_h	Period of F_h fan construction (11.3 ± 2.3 kyr)
ϵ_p	Middle–Late Pleistocene denudation rates
ϵ_h	Holocene total denudation rates
ϵ_c	Holocene denudation rates in the piedmont
ϵ_r	Holocene denudation rates in the range

to another, and the distinction between the Pleistocene and Holocene features (fans, canyons) is not always considered. In addition, these documents mostly focus on the central part of the piedmont only. Therefore, to perform a study on the whole piedmont and to accurately locate the outlines of the fans F_p and F_h and their respective catchment areas, two new morpho-sedimentary maps based on satellite images, digital elevation model and field observations were drawn. One concerns the Late Pleistocene landscape (Figure 4) and the other one the present-day landscape (Figure 5). The map construction and uncertainties are detailed in Appendix A. These maps enabled the extraction of the drainage basins and fan outlines for the two periods (KMZ coordinates given in Supplementary Data S2, S3, S4 and S5) and their areas (Tables II and III). Note that in this study only the 10 catchment–fan systems for which the position of the basal surface of the fans F_p could be identified in the field were considered.

Volumes of sediments

Fan outlines

Given their growth dynamics, the outlines of the fans F_p and F_h can be used to map the extent of both their top and basal surfaces. Outline elevations were extracted from the ASTER DEM (~10 m vertical resolution) with a point every meter, and interpolated when required (e.g. where fan outlines have been eroded or covered by other deposits). Finally, a sliding window over 10 m was applied to the dataset in order to filter the DEM noise.

Fan top surfaces

For the two fan generations, the top surface elevations were extracted from the ASTER DEM with a grid resolution of 250 m. Here again, data were interpolated to recover the original fan surface over the areas of the fan surface 'damaged' by posterior erosion and deposition, or by human land uses. Two different interpolation schemes (linear or cubic) were used in order to quantify the error associated with the interpolation method. The final fan top surface was then obtained on a 250 × 250 m model grid (Figure 6a, b).

Fan basal surfaces

The basal surfaces of the Middle–Late Pleistocene fans were reconstructed from field surveys along the river canyons. As explained above, the rivers of the northern Chinese Tian Shan have incised the fans F_p during the Holocene. In the cliffs surrounding the streams, the F_p basal surfaces are often identifiable, due to contrasts in sediment colour, lithology or dip between the fan deposits and older series (Figure 3). However, the further from the relief, the more difficult this identification as the contrasts become less and less marked (see Appendix B.1 for details on outcrop identification and data acquisition). Consequently, the F_p basal surface outcrops were mostly identified close to the fan apexes or to the anticlines in the piedmont (Figure 7a, b; Data S6).

The F_p basal surfaces were modelled from this dataset on the basis of two hypothesis. First, in agreement with field observations (Figure 3b), we considered that the basal surfaces are parabolic in transverse cross-section (Figure 7c). Then, we assumed that the basal surfaces are regular between two points and that there is no major tectonic or topographic structure hidden underneath the fans (Figure 7d). Finally, the interpolation methods presented for the top surface reconstruction were used to model the fan basal surfaces over 250 × 250 m model grids (Figure 6c).

As the Holocene fans have not been incised, the position of their basal surface could not be determined from direct observation. Therefore, we considered that fans F_h were built over a topography composed of two gently sloping surfaces: the surface of the fans F_p (slope ~1–2.5%) followed to the north by the downstream alluvial plain (slope ~0.2–0.4%), in agreement with (Jolivet *et al.*, 2014). Here again, the methods of interpolation described above were implemented to model the F_h basal surfaces over 250 × 250 m grids (Figure 6d).

Fan and sediment volumes

Fan thickness maps were built as the difference in elevation between the reconstructed top and basal surfaces of the fans. The thickness on each cell, *h*, was defined as the mean value

Copyright © 2016 John Wiley & Sons, Ltd.

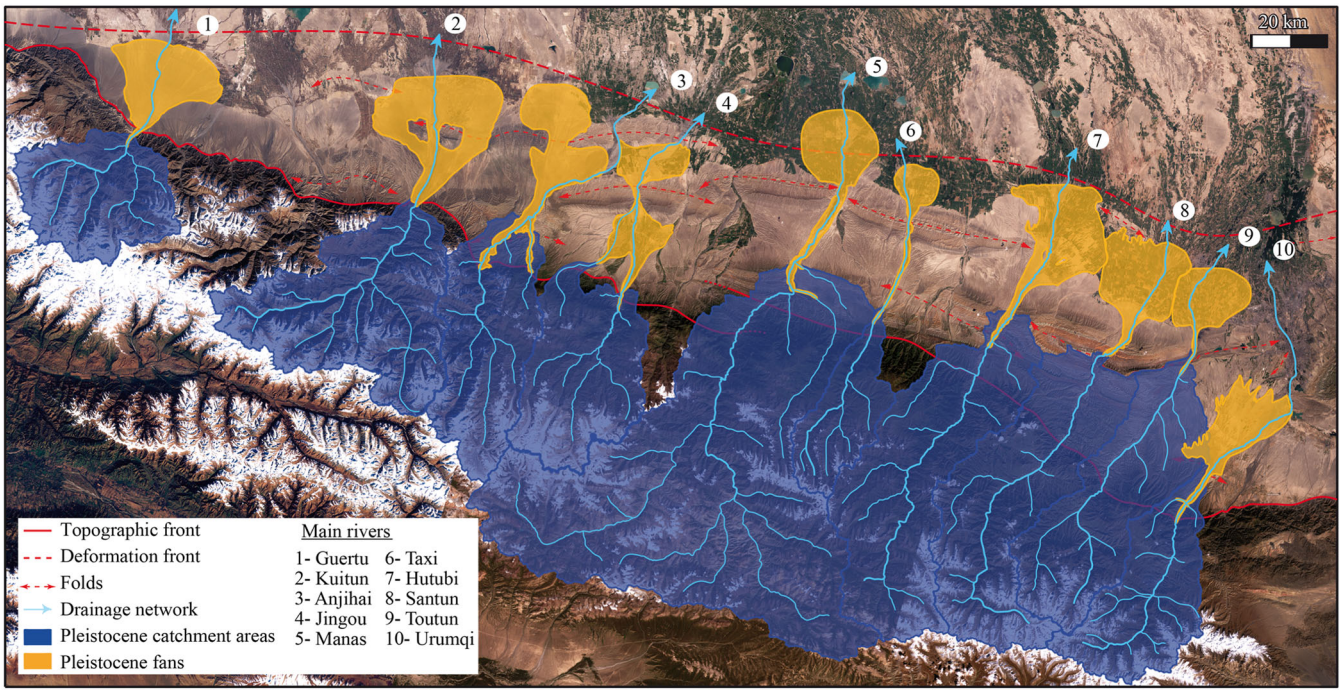

Figure 4. Late Pleistocene morpho-sedimentary map of the northern side of the Chinese Tian Shan. The Middle–Late Pleistocene fans F_p (in orange) are presented with their catchment areas (in dark blue). See text for details about the map construction. This figure is available in colour online at www.interscience.wiley.com/journal/espl.

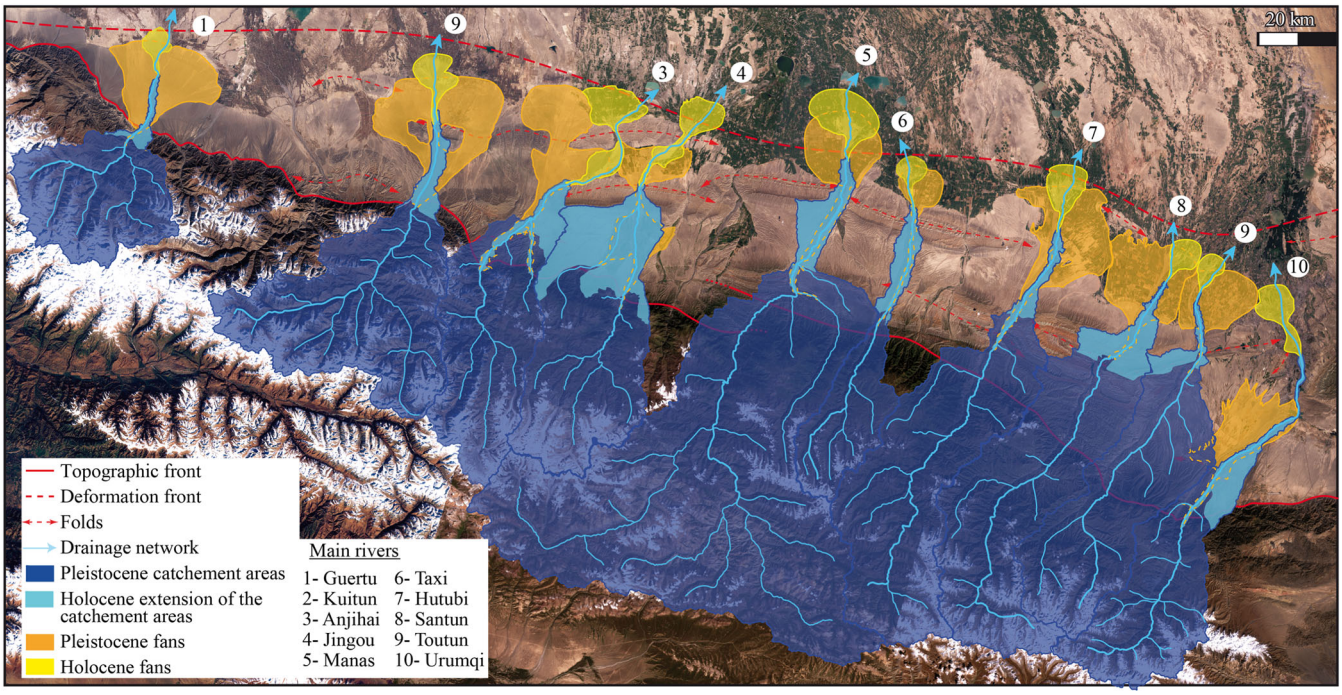

Figure 5. Present-day morpho-sedimentary map of the northern side of the Chinese Tian Shan. The Holocene fans F_h (in yellow) are presented with their catchment areas (long-standing part in dark blue and Holocene extension in light blue). See text for details about the map construction. This figure is available in colour online at www.interscience.wiley.com/journal/espl.

obtained by the two interpolation methods. The total volume of a fan, V_F, was calculated by the addition of the individual volumes of each cell (Tables II and III; Figure 6e, f). The volume of sediments trapped in fans, $V_{\lambda F}$, is then the volume V_F corrected for the porosity of the deposits λ (Tables II and III; see Appendix B.2 for details on the volume reconstruction and uncertainties). As the simplest geometry was used to reconstruct the F_h basal surfaces (i.e. a sharp transition between the F_p fan and plain slopes), Holocene volumes correspond to maximum estimates.

From sediment volumes to denudation rates

The denudation rate, ϵ, of a given area was calculated from the volume of sediments trapped in the associated fan $V_{\lambda F}$ through a simple mass conservation law:

$$\epsilon = \frac{V_{\lambda F}}{\alpha \times A_d \times P}$$

where α is the proportion of river sediment load trapped in the fan, A_d is the drainage basin area of interest, and P is the

Copyright © 2016 John Wiley & Sons, Ltd.

Table II. Morpho-sedimentary parameters of the Middle–Late Pleistocene catchment–fan systems. A_{dp} is the catchment area, A_{F_p} the fan area, V_{F_p} the fan volume, and $V_{\lambda F_p}$ the volume of sediments trapped in the fan. Δ are the uncertainties associated with each parameter

River (W to E)	A_{dp} (km^2)	ΔA_{dp} (km^2)	A_{F_p} (km^2)	ΔA_{F_p} (km^2)	V_{F_p} (km^3)	ΔV_{F_p} (km^3)	$V_{\lambda F_p}$ (km^3)	$\Delta V_{\lambda F_p}$ (km^3)
Guertu	1056	8	419	4	13	0.7	10.4	1.6
Kuitun	1926	14	597	7	29.2	0.6	23.4	2.8
Anjihai	1340	10	471	4	14.4	0.6	11.5	1.6
Jingou	1321	10	336	4	6.4	0.4	5.1	0.8
Manas	5356	40	381	4	9.1	0.2	7.3	0.9
Taxi	632	5	141	2	3.2	0.0	2.6	0.3
Hutubi	2150	16	480	5	15.7	0.6	12.6	1.8
Santun	1996	15	416	5	8.3	0.3	6.6	0.9
Toutun	1597	12	264	2	7.7	0.1	6.2	0.7
Urumqi	1115	8	323	2	5.2	0.1	4.2	0.5
Average	**1850**	**14**	**383**	**4**	**11.2**	**0.4**	**9.0**	**1.2**

Table III. Morpho-sedimentary parameters of the Holocene catchment–fan systems. Q_w is the present-day river average annual discharge, A_{dh} the catchment area, A_{F_h} the fan area, V_{F_h} the fan volume and $V_{\lambda F_h}$ the volume of sediments trapped in the fan. Δ are the uncertainties associated with each parameter

River (W to E)	Q_w (m^3/s)	A_{dh} (km^2)	ΔA_{dh} (km^2)	A_{F_h} (km^2)	ΔA_{F_h} (km^2)	V_{F_h} (km^3)	ΔV_{F_h} (km^3)	$V_{\lambda F_h}$ (km^3)	$\Delta V_{\lambda F_h}$ (km^3)
Guertu	/	1111	8	45	1	0.4	0.1	0.3	0.1
Kuitun	20	2049	15	98	1	2.4	0.3	1.9	0.4
Anjihai	9.8	1512	11	189	2	3.6	0.5	2.9	0.7
Jingou	10.2	1906	14	133	1	2	0.3	1.6	0.4
Manas	40.5	5594	42	182	1	1.8	0.2	1.4	0.3
Taxi	7.2	782	6	46	1	0.7	0.1	0.6	0.1
Hutubi	15.1	2275	17	102	1	1.1	0.1	0.9	0.1
Santun	9.9	2250	17	57	1	0.6	0.0	0.5	0.0
Toutun	7.4	1701	13	43	1	1	0.0	0.8	0.1
Urumqi	7.5	1318	10	102	1	1.2	0.1	1.0	0.2
Average	**14.2**	**2050**	**15**	**100**	**1**	**1.5**	**0.2**	**1.2**	**0.3**

duration of the fan construction (see Appendix C for details on the denudation rate uncertainties).

As the fans are made up of conglomerates (i.e. typical bedload deposits), we considered that they have trapped all the bedload sediments transported by the rivers. A value of 17.3 ± 0.3% was thus used for α on the basis of the only sediment load measurements performed in the region (Liu *et al.*, 2011).

As the rivers have deeply incised the piedmont at the onset of the Holocene (Figure 8), a large amount of matter has been removed from the fans F_p to feed the fans F_h. This contribution to the sediment fluxes is not negligible. For example, Jolivet *et al.* (2014) have suggested that the Holocene fan of the Kuitun River could be entirely made up of sediments reworked from the piedmont. Therefore, the volume of sediments issued from the piedmont during the Holocene and from the long-standing part of the catchment areas (the one inside the range, which already existed at the end of the Pleistocene) must be estimated to characterize the evolution of the denudation rates of the range through time. The volumes of sediments recycled from the piedmont correspond to the volumes of the canyons excavated by the rivers. As the incisions are deep and vertical (of the order of several hundred metres; Figure 8), we regarded the canyon cross-sections as rectangular and did not include the uppermost terraces. This implies that the reconstructed volumes of the canyons are minimum estimates.

The average length, width and depth of these structures were measured from the DEM and used to calculate the corresponding volumes V_c (Table IV). These volumes were corrected for the sediment porosity to assess the volumes of matter, $V_{\lambda c}$,reworked from the canyons (Table IV). As a major part of the incised deposits corresponds to conglomerates of the fans F_p, the same porosity λ of 20 ± 10% was used. It was possible to propose a Holocene denudation rate in the piedmont resulting from this sediment recycling based on the volumes $V_{\lambda c}$ divided by the areas of the Holocene drainage basin extensions, $A_{d,h-p}$ (i.e. the Holocene catchment areas minus the Late Pleistocene ones), and the incision duration, P_h. In addition, the volumes of matter reworked from the canyons were also subtracted from the volumes of sediments trapped in fans F_h in order to estimate the remaining volumes of sediments, V_{λ,F_h-c}, coming from upstream. Once corrected for the sediment partitioning, these volumes were used to calculate the denudation rates of the long-standing parts of the catchment areas.

The same process of incision and reworking could have happened when the fans older than the Middle–Late Pleistocene ones were abandoned, but no information exists on that point. Accordingly, the volumes of sediments trapped in the fans F_p should be considered as maximum estimates. Similarly, the volumes of sediments trapped in the fans F_h and the volumes exported from the Holocene canyons are respectively maximized and minimized due to the geometric simplifications. In consequence, the denudation rates assessed in this study for both periods correspond to maximum values.

Copyright © 2016 John Wiley & Sons, Ltd.

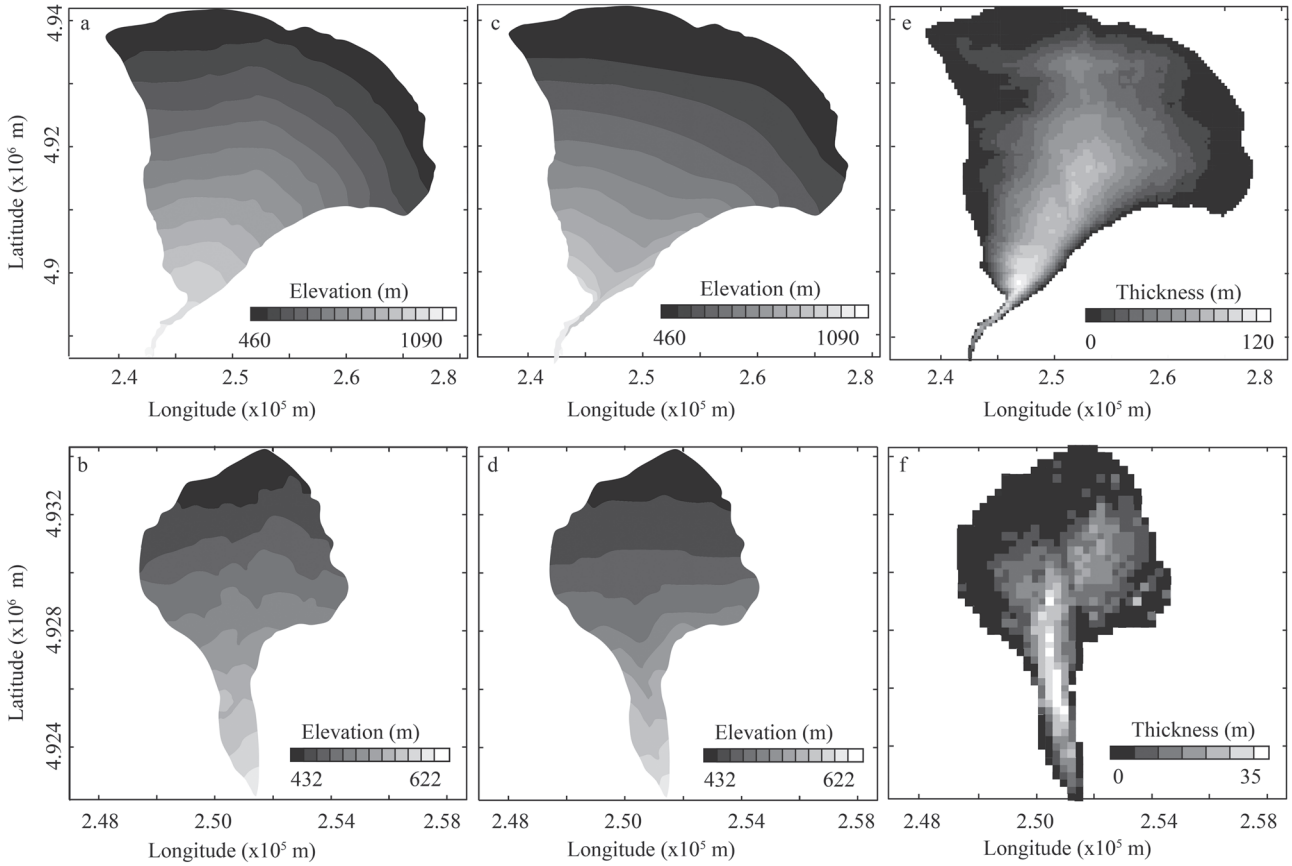

Figure 6. Example of geometric reconstructions for the fans of the Guertu River. Reconstruction of the (a, b) top surfaces, (c, d) basal surfaces and (e, f) sediment thicknesses of the Middle–Late Pleistocene and Holocene fans, respectively.

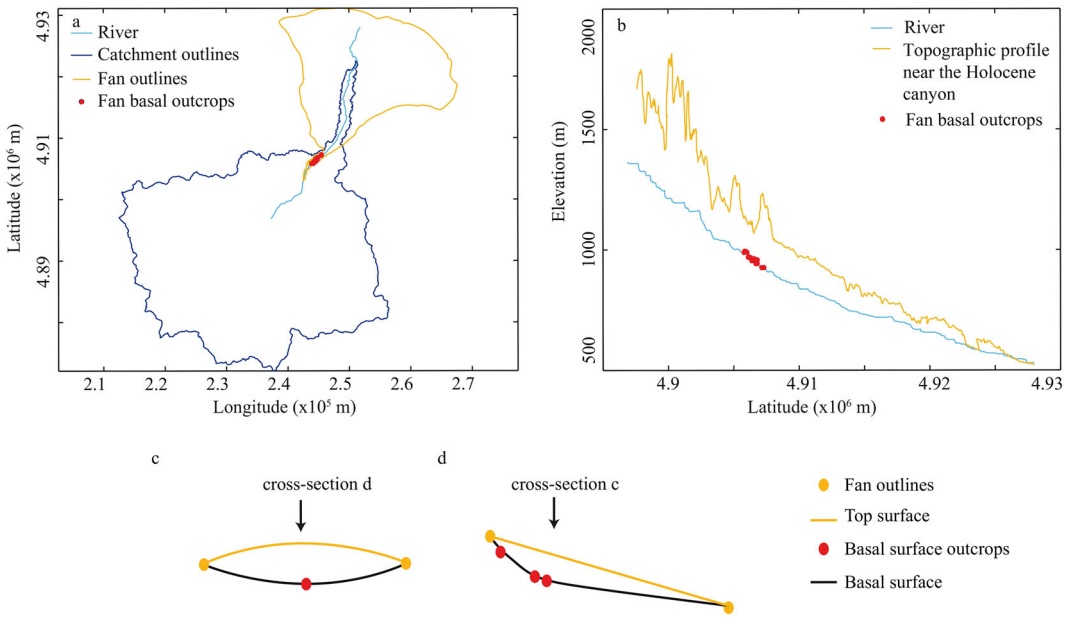

Figure 7. Location of the Middle–Late Pleistocene fan basal surface outcrops (red dots) along the Guertu River (light-blue line) (a) in plan view and (b) in cross-section. Diagrams illustrating the geometric hypothesis used to reconstruct the basal surfaces in (c) transverse and (d) longitudinal cross-sections. See text for explanation. This figure is available in colour online at www.interscience.wiley.com/journal/espl.

Results

Morpho-sedimentary characteristics of the catchment–fan systems

The two morpho-sedimentary maps (Figures 4 and 5) focus on the 10 catchment–fan systems for which the basal surface of the Middle–Late Pleistocene fans F_p could be identified in the field, namely from west to east: the Guertu, Kuitun, Anjihai, Jingou, Manas, Taxi, Hutubi, Santun, Toutun and Urumqi systems (called after the main stream names given in Zhou *et al.*, 1999). These maps display features of the Late Pleistocene and present-day landscapes in the studied area, namely the fans F_p and F_h, and the associated catchment areas with their long-standing part and their recent extension (Figures 4 and 5). In addition to the catchment–fan system outlines, the

Copyright © 2016 John Wiley & Sons, Ltd.

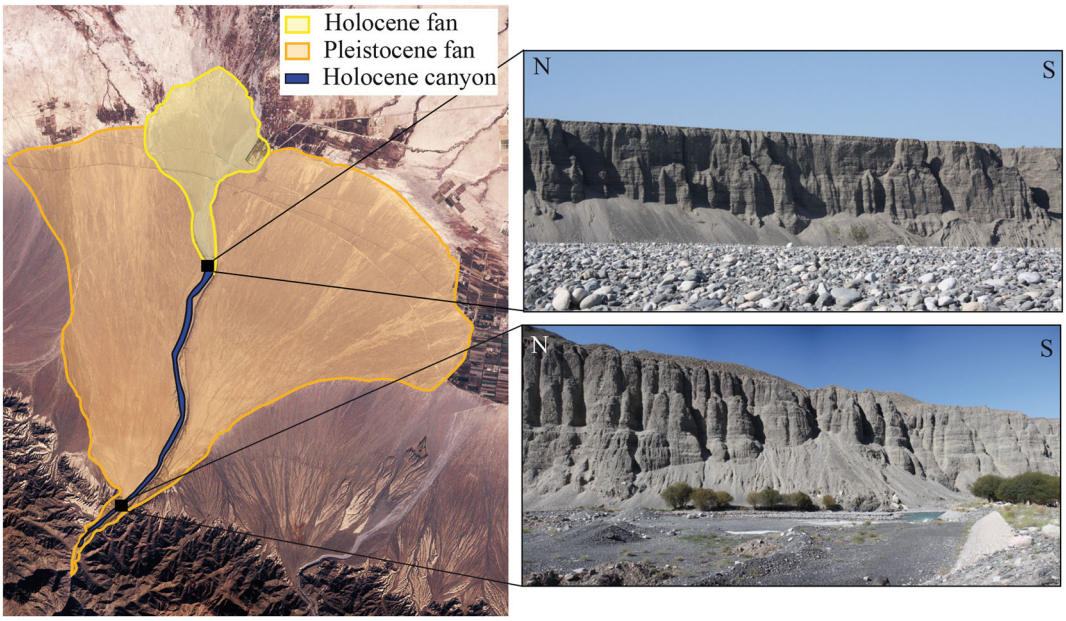

Figure 8. Morphology of the Holocene canyon of the Guertu River in map view (Landsat picture) and in lateral view (field pictures taken from the present-day river bed). The cliffs are ~50 m high. This figure is available in colour online at www.interscience.wiley.com/journal/espl.

Table IV. Morpho-sedimentary parameters associated with the Holocene extension of the drainage basins. $A_{d,h-p}$ is the area of the Holocene drainage basin extension with the corresponding increase in percent, V_c the volume of the Holocene canyon dug into the Middle-Late Pleistocene fan, $V_{\lambda c}$ the volume of sediments removed from the canyon and V_{λ,F_h-c} the volume of sediments exported out of the range. Δ are the uncertainties associated with each parameter

River (W to E)	$A_{d,h-p}$ (km^2)	$\Delta A_{d,h-p}$ (km^2)	V_c (km^3)	ΔV_c (km^3)	$V_{\lambda c}$ (km^3)	$\Delta V_{\lambda c}$ (km^3)	V_{λ,F_h-c} (km^3)	$\Delta V_{\lambda,F_h-c}$ (km^3)
Guertu	55 (+5%)	16	0.4	0.1	0.3	0.1	0	0.2
Kuitun	123 (+6%)	29	2.7	0.5	2.1	0.4	0	0.8
Anjihai	172 (+13%)	21	1.6	0.3	1.3	0.2	1.6	0.7
Jingou	585 (+44%)	24	0.6	0.1	0.5	0.1	1.1	0.5
Manas	238 (+4%)	82	0.6	0.1	0.5	0.1	0.9	0.4
Taxi	150 (+24%)	11	0.1	0.0	0.1	0.0	0.5	0.1
Hutubi	125 (+6%)	33	0.4	0.2	0.3	0.1	0.6	0.3
Santun	254 (+13%)	32	0.2	0.0	0.2	0.0	0.3	0.0
Toutun	104 (+7%)	25	0.1	0.0	0.1	0.0	0.7	0.1
Urumqi	203 (+18%)	18	0.6	0.1	0.5	0.1	0.5	0.2
Average	**201 (+11%)**	**29**	**0.9**	**0.2**	**0.6**	**0.1**	**0.6**	**0.3**

topographic and deformation fronts as well as the main folds are indicated.

During the Middle–Late Pleistocene, the drainage basins are mostly located in the hinterland mountains. Their areas range from 632 ± 5 km^2 for the Taxi catchment–fan system to 5356 ± 40 km^2 for the Manas one, with an average area of 1850 ± 14 km^2 (Table II). The associated alluvial fans F_p are located both in the piedmont and the foreland basin, and their areas range from 141 ± 2 km^2 for the Taxi system to 597 ± 7 km^2 for the Kuitun one, with an average of 382 ± 4 km^2 (Table II). In terms of volume, these fans store between 2.6 ± 0.3 and 23.4 ± 2.8 km^3 of sediments (for the Taxi and Kuitun fans, respectively), with an average volume of 9.0 ± 1.2 km^3 (Table II). In most cases, their thickness is maximal at their apex, with up to 120 m thick deposits (Figure S1).

During the Holocene, the catchment areas expanded in the piedmont due to the downstream propagation of an erosion wave triggered by changes in water and/or sediment discharges (Poisson, 2002; Poisson and Avouac, 2004). Consequently, the Holocene drainage basins are larger than the Middle–Late Pleistocene ones, ranging from 782 ± 6 km^2 for the Taxi system to 5594 ± 42 km^2 for the Manas one, with an average of 2050 ± 42 km^2 (Table III). The Holocene extensions of these drainage basins correspond to an increase in size of 4% for the Manas system and up to 44% for the Jingou one, with an average of 11% (Table IV).

Owing to the propagation of the erosion–sedimentation boundary down the river systems, the alluvial fans F_h are mostly located in the foreland basin at the toe of the fans F_p. Contrary to the catchment areas, the fans F_h are smaller than the fans F_p. Their areas range from 43 ± 1 km^2 for the Toutun fan to 189 ± 2 km^2 for the Anjihai one, with an average of 100 ± 1 km^2 (Table III). In terms of volume, they contain between 0.3 ± 0.1 and 2.9 ± 0.7 km^3 of sediments (for the Guertu and Anjihai fans, respectively) with an average volume of 1.2 ± 0.3 km^3 (Table III). In these fans, the sediment thickness is maximal at the slope break between the fans F_p and the downstream alluvial plain, with up to 90 m thick deposits (Figure S2).

Copyright © 2016 John Wiley & Sons, Ltd.

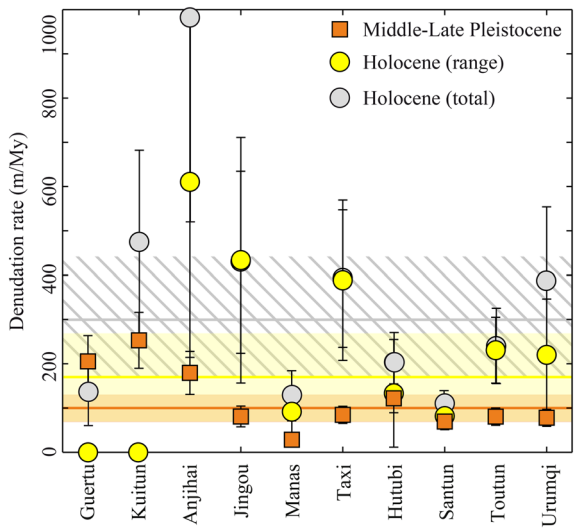

Figure 9. Denudation rates along the northern side of the Chinese Tian Shan. The Middle–Late Pleistocene denudation (orange squares) varies between 30 ± 10 and 250 ± 60 m/Myr, with an average value (orange line) of 100 ± 30 m/Myr (Table **??**). The total Holocene denudation (grey dots) varies between 130±60 and 970±460 m/Myr, with an average value of 300 ± 130 m/Myr (grey line). However, the denudation in the range only (yellow dots) varies from 0 to 610 ± 400 m/Myr, with an average value (yellow line) of 170 ± 110 m/Myr (Table IV). This figure is available in colour online at www.interscience.wiley.com/journal/espl.

Denudation rates

During the Middle–Late Pleistocene

The Middle–Late Pleistocene denudation rates, ϵ_p, were calculated as

$$\epsilon_p = \frac{V_{\lambda F_p}}{\alpha \times A_{dp} \times P_p}$$

$_p$ referring to the Middle–Late Pleistocene values estimated from the morpho-sedimentary maps and from the literature (see 'Data and Methodology', above). These denudation rates range from 30 ± 10 m/Myr for the Manas system to 250 ± 60 m/Myr for the Kuitun one, with an average value of 100 ± 30 m/Myr (Table V and Figure 9). One may notice that ϵ_p varies within almost a factor of 10 between the different drainage basins.

During the Holocene

The total denudation rates for the Holocene, ϵ_h, were calculated as follows:

$$\epsilon_h = \frac{V_{\lambda F_h}}{\alpha \times A_{dh} \times P_h}$$

$_h$ referring to the Holocene values. These total rates range from 110 ± 40 m/Myr for the Santun system to 970 ± 460 m/My for the Anjihai one, with an average value of 300 ± 130 m/Myr (Table V and Figure 9). Here again, a factor of 10 is observed between the different rates. However, to discuss the evolution of the denudation rates from the Middle–Late Pleistocene to the Holocene, the denudation in the piedmont must be differentiated from the denudation in the mountain range.

The denudation rates in the piedmont, ϵ_c, were calculated as the volumes of sediments removed from the canyons artificially spread over the Holocene extensions of the drainage basins:

$$\epsilon_c = \frac{V_{\lambda c}}{A_{d,h-p} \times P_h}$$

As these rates are calculated from eroded volumes and not from deposited ones, α is not required in this equation. Values range from 60 ± 20 m/Myr for the Taxi system to 1550 ± 780 m/Myr for the Kuitun one with, on average, 260 ± 130 m/Myr (Table V). On the other hand, considering the remaining volumes of sediments in the fans F_h and the long-standing part of the drainage basins, the denudation rates in the range, ϵ_r, were calculated as follows:

$$\epsilon_r = \frac{V_{\lambda,F_h-c}}{\alpha \times A_{dp} \times P_h}$$

These denudation rates range from 0 m/Myr for the Guertu and Kuitun systems to 610 ± 400 m/Myr for the Anjihai one, with an average value of 170 ± 110 m/Myr (Table V and Figure 9).

The Holocene denudation in the piedmont results from sediment reworking linked to the river incision at the onset of the last deglaciation, which is a local and probable short-term contribution. The denudation in the range should be more representative of the regional and long-term rate and is therefore the relevant value to compare the Middle–Late Pleistocene and Holocene periods. It did not noticeably evolve through time, with average values weighted by the drainage areas of 100 ± 30 m/Myr and 170 ± 100 m/Myr respectively (Figure 9).

Finally, these calculations lead to an average denudation rate of ∼135 m/Myr for the northern Tian Shan for the last 300 kyr. Since the sediment volumes have systematically been maximized, this rate is a maximum estimate.

Discussion

Catchment–fan mass balance

Denudation rates issued from catchment–fan mass balances are subject to several sources of uncertainty. In addition to the volumes of sediments and areas of the drainage basins, the duration of fan construction P and the fraction of the river sediment load trapped in the fans α must be determined. In most cases, the volumes and areas, as well as their uncertainties, can be accurately quantified. In this study, these uncertainties related to the geometry of the system are very small (less than 2%) and could have been neglected. In contrast, the values of P and α are not so well constrained because they require strong field efforts and access to the whole drainage system to be characterized.

The published time constraints for the northern side of the Chinese Tian Shan are scarce compared to the number and size of the fans (Molnar *et al.*, 1994; Poisson, 2002; Poisson and Avouac, 2004; Lu *et al.*, 2010; Yang *et al.*, 2013; Gong *et al.*, 2014). Yet the fan onset and abandonment seem to vary across space from a few thousand years and it would be important to quantify better this variability because of its potential impact on denudation rate assessment. For the Holocene, a variation of a few thousand years over P_h (∼11.3 kyr) would imply a drop or rise of the denudation rates by a factor of up to 2. On the contrary, for the Middle–Late Pleistocene, this variability has no major impact on the determination of the denudation rates as it is an order of magnitude smaller than P_p (∼277 kyr).

The sediment partitioning, which is quite difficult to estimate, is the other main critical parameter in such mass balance studies. In this work, we considered that the alluvial fans are built by the deposition of the entire bedload. The only data available in the region were used to define the fraction of sediments transported as bedload (∼17%) compared to the total river load (Liu *et al.*, 2011). As the potential variation from

Copyright © 2016 John Wiley & Sons, Ltd.

Table V. Denudation rates for the 10 catchment–fan systems considered in this study. ϵ_p is the Middle–Late Pleistocene denudation rate in the range, ϵ_h the total Holocene denudation rate, ϵ_c the Holocene denudation rate in the piedmont and ϵ_r the Holocene denudation rate in the range. Values are rounded to the nearest tenth and averages are pondered by the drainage areas. Δ are the uncertainties associated with each parameter

River (W to E)	ϵ_p (m/Myr)	$\Delta\epsilon_p$ (m/Myr)	ϵ_h (m/Myr)	$\Delta\epsilon_h$ (m/Myr)	ϵ_c (m/Myr)	$\Delta\epsilon_c$ (m/Myr)	ϵ_r (m/Myr)	$\Delta\epsilon_r$ (m/Myr)
Guertu	210	60	150	90	510	290	0	20
Kuitun	250	60	480	220	1550	780	0	50
Anjihai	180	50	970	460	660	330	610	400
Jingou	80	20	430	210	70	40	430	280
Manas	30	10	130	60	180	90	90	60
Taxi	80	20	370	170	50	20	390	180
Hutubi	120	30	200	80	220	190	130	120
Santun	70	20	110	40	60	20	80	30
Toutun	80	20	240	80	70	20	230	80
Urumqi	80	20	370	150	210	100	220	130
Average	**100**	**30**	**300**	**130**	**260**	**130**	**170**	**110**

one basin to another could not be quantified, uncertainty on this ratio relates to measurements only. However, other studies on gravel-bed rivers indicate that the bedload can represent 10–50% of their total load (Lane and Borland, 1951; Meunier *et al.*, 2006; Schiefer *et al.*, 2010). With such ratios, the average denudation rate of the northern Tian Shan since 300 kyr could be between 50 and 230 m/Myr. It is also possible that fans are built by a fraction of the total load that does not correspond exactly to the entire bedload. Studies on sediment partitioning in alluvial systems suggest that 25–80% of the solid load of a river can be deposited in alluvial fans (Kiefer *et al.*, 1997; Oguchi, 1997; Jolivet *et al.*, 2014). In the Urumqi River, the solid load represents ~53% of the total load (Liu *et al.*, 2011). Extrapolating this ratio to the other rivers of the piedmont implies that the fans could have trapped ~12–38% of the total load. With such ratios, the average denudation rate could be between 60 and 200 m/Myr.

Further work is thus strongly required to determine better the sediment transport and partitioning in alluvial systems. Yet, in the northern Tian Shan, the values discussed previously show that the average denudation rate cannot exceed a few hundreds of metres per million years for the last 300 kyr.

Denudation in the northern Chinese Tian Shan

At a local scale, the catchment–fan mass balances show that the denudation rate varies from one drainage basin to another (Figure 9) but it is difficult to understand what controls this variability. It could result from changes in space of the forcing factors, but the potential variations of tectonic and climatic conditions over the studied area are not known. Therefore, their influence on the denudation variability cannot be discussed. Instead, the relationship between denudation rates and some geomorphic characteristics of the drainage basins can be studied, such as the drainage area, mean elevation, mean slope and channel steepness index. These parameters are generally considered as proxies in a broad way for sediment production and transport (e.g. Ahnert, 1970; Summerfield and Hulton, 1994; Hovius, 1998; von Blanckenburg, 2005). However, the correlation between denudation rates and basin morphometrics in the northern Tian Shan is poor (Figure S3). Such a scattering could be due to differences in bedrock properties (e.g. in lithology, fracturing, dip, foliation) and erodibility, vegetation cover, glacial processes and/or sediment transport efficiency (e.g. de Vente *et al.*, 2007; Insel *et al.*, 2010; Norton *et al.*, 2011; Torres Acosta *et al.*, 2015). In the studied area, these factors are likely to vary from one drainage basin to another with, for example, different proportions of Palaeozoic igneous rocks, Palaeozoic carbonates and Meso-Cenozoic clastic sediments affected by a more or less complex tectonic history. Vegetation could also vary a lot with different proportions of bare rock/soils, herbaceous plants and trees that could influence the sediment production and transport. In addition, denudation rates could be influenced by glacial erosion or morphological heritage, as well as sediment storage that has been evidenced in the drainage basins (Li *et al.*, 2001; Jolivet *et al.*, 2014). Unfortunately, these basins are poorly accessible and all those factors are very difficult to quantify in this region. Finally, changes in sediment production, transport and deposition should also influence the sediment partitioning, and therefore, α might vary from one catchment area to another. The determination of this parameter for all the basins over the considered periods could be a way to assess whether or not differences in the parameters mentioned previously (e.g. lithology, vegetation) are the sources of the denudation variability. However, to date, there is no method to perform such measurement. Further work would be of interest to understand better what influence catchment–fan mass balance and the denudation rates at the local scale.

At a regional scale, the average denudation rate in the mountain range seems to be around 135 m/Myr for the last 300 kyr. This value is in good agreement with previous mass balance estimates performed at different scales (Figure 10). Using the same approach applied to one Holocene catchment–fan system and on the solid sediment load only, Jolivet *et al.* (2014) suggest a rate lower than 100 m/Myr for the last 12 kyr. From a sediment budget over the whole Junggar basin, Métivier and Gaudemer (1997) propose a long-term regional denudation of ~40 m/Myr since 6 Myr. From sediment load measurements in one river during 2 years, Liu *et al.* (2011) determine a short-term and local denudation of ~20 m/Myr. Studies in the same area based on cosmogenic analysis point toward higher average values of 200 to 600 m/Myr for the last 8 Myr (Charreau *et al.*, 2011; Puchol, 2013). However, cosmogenic concentrations are influenced by the distribution of the sources or of the samples in the drainage basin (nearby an active fault or a glacier), by the story of the sediment transport and also by a possible unsteady erosion that could lead to maximize denudation rates (Jolivet *et al.*, 2014; Carretier *et al.*, 2015). Finally, basement-derived fission track ages indicate

Copyright © 2016 John Wiley & Sons, Ltd.

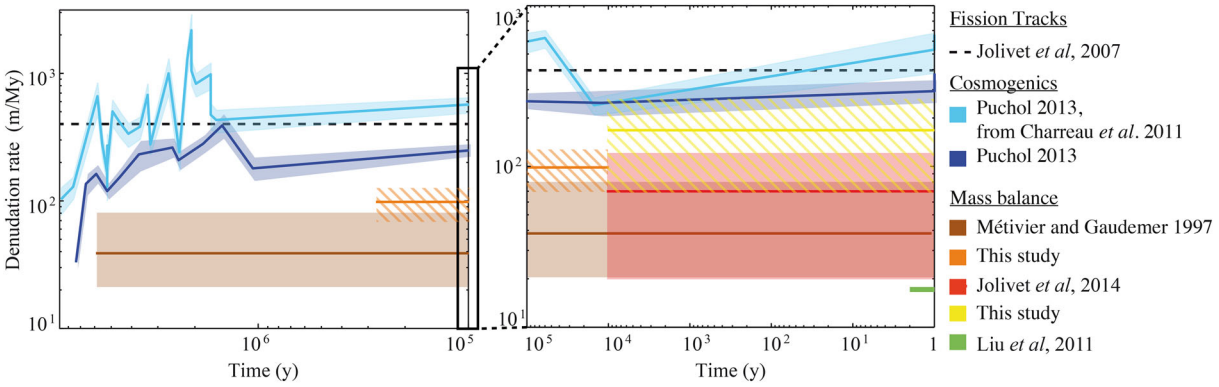

Figure 10. Existing estimates for denudation rates of the northern side of the Chinese Tian Shan (from (Jolivet *et al.*, 2007; Métivier and Gaudemer, 1997; Charreau *et al.*, 2011; Liu *et al.*, 2011; Puchol, 2013; Jolivet *et al.*, 2014); this study). This figure is available in colour online at www.interscience.wiley.com/journal/espl.

that the northern Tian Shan (Borohoro range) rose between 15 and 10 Ma ago (Dumitru *et al.*, 2001; Jolivet *et al.*, 2010). Considering a maximum geothermal gradient of 30∘ C/km, these ages correspond to 4 km of rock exhumation, leading to an average erosion of 260–400 m/Myr for this period (Figure 10). However, erosion rates derived from apatite fission track data rely largely on the understanding of the geothermal gradient and the behaviour of the isotherms (i.e. their capacity to re-equilibrate) during tectonic deformation (e.g. Ehlers and Farley, 2003). In other words, the rates determined by cosmogenic and thermochronological methods in the Tian Shan might correspond to maximum possible values. Consequently, only the values determined by mass balances are considered in this study to determine the average denudation rate for this range. They all converge toward a few hundreds of metres per million years at maximum regardless of the space or time scale.

Influence of tectonics and climate

For the whole northern side of the Tian Shan (range and piedmont), the average denudation rate rises from ∼100 m/Myr during the Middle–Late Pleistocene to ∼300 m/Myr during the Holocene (Table V and Figure 9). This increase is a direct consequence of the downstream extension of the catchment areas associated with sediment reworking due to the last glacial–interglacial transition (Molnar *et al.*, 1994; Poisson, 2002; Poisson and Avouac, 2004; Lu *et al.*, 2010; Gong *et al.*, 2014). Over the last 300 kyr, the evolution of the sediment fluxes from the Tian Shan to the Junggar Basin is thus clearly climate-driven, as observed in other places at the same period (Church and Ryder, 1972; Church and Slaymaker, 1989; Delmas *et al.*, 2015). However, once corrected for this sediment recycling, the average denudation rates in the long-standing part of the drainage basins are quite similar for the two periods (∼100 and ∼170 m/Myr). The consistency between these rates and those previously published (Métivier and Gaudemer, 1997; Charreau *et al.*, 2011; Liu *et al.*, 2011; Puchol, 2013; Jolivet *et al.*, 2014) suggests that the pulse observed at the onset of the Holocene is a local and transient feature associated with a major morphological evolution that did not affect the denudation of the hinterland mountains (see also ; Jolivet *et al.*, 2014).

As mentioned previously, an average rate of a few hundred metres per million years seems to be more representative of the denudation intensity in the mountain range whatever the considered space and time scales. This rate is quite low for a high and active mountain belt like the northern Tian Shan, as it is closer to the rates observed in the flat Middle Europe (Schaller *et al.*, 2001; Hoffmann *et al.*, 2007) than to those observed in the Himalayas (Bhutiyani, 2000; Galy and France-Lanord, 2001; Grujic *et al.*, 2006; Vance *et al.*, 2003) (Table VI). To discuss whether this low rate is controlled by tectonics or climate, recent shortening rate and precipitations can be used as respective proxies for the two forcings in different mountain ranges throughout the world. Recent shortening rate in the Chinese Tian Shan is around ∼1 cm/yr (Reigber *et al.*, 2001; Champagnac *et al.*, 2012) and seems to have been stable for the last million years (Avouac *et al.*, 1993; Burtman *et al.*, 1996; Burchfiel *et al.*, 1999; Charreau *et al.*, 2009b). Present-day precipitation is around 300 mm/yr (Métivier and Gaudemer, 1997; Poisson, 2002; Sobel *et al.*, 2003). Their amount might have varied over the last million years since alternations of drier and wetter periods are documented in the region at different time scales (Molnar *et al.*, 1994; Rhodes *et al.*, 1996; Poisson and Avouac, 2004; Yi *et al.*, 2004; Gallaud, 2008; Xu *et al.*, 2010). However, in spite of these variations, the average denudation rate is always low (i.e. less than a few hundred metres per million years) whatever the time scale over which it is integrated: 2 years (Liu *et al.*, 2011), the Holocene (Jolivet *et al.*, 2014, and this study), the last 300 kyr (this study) or a few million years (Metivier and Gaudemer, 1999; Charreau *et al.*, 2011).

First, the denudation rates according to the shortening rates are compared in ranges where the precipitation rates are equivalent (∼300 mm/yr; Table VI and Figure 11a). Denudation rates increase slightly with the shortening rate (from ∼30 to ∼135 m/Myr), but stay within the same order of magnitude. In these semi-arid areas, the denudation rate is systematically low. Next, the denudation rates according to the annual precipitation rates are compared in ranges where the shortening rates are equivalent (∼1 cm/yr; Table VI and Figure 11b), excluding orogenic plateaus to avoid a topographic bias. Two groups clearly appear: (i) ranges with limited rainfall (<1000 mm/yr), where the denudation rates are low (∼100 m/Myr); versus (ii) ranges with higher precipitations (>1000 mm/yr), where the denudation rates are one order of magnitude higher (>1000 m/Myr). In other words, an increase of one order of magnitude in the shortening rate in a semi-arid climate induces a limited change of the denudation rate. On the contrary, a rise of one order of magnitude in the precipitation rate in equivalent shortening velocity areas induces a similar increase of the denudation rate. Therefore, we propose that the low denudation rate observed in the Tian Shan is due to the aridity of the region.

Dry climatic conditions are attested in this area for longer than the period documented for the denudation. The Cenozoic

Copyright © 2016 John Wiley & Sons, Ltd.

Table VI. Precipitation, shortening and denudation rates of some mountain ranges over the world

Setting	Precipitations (mm/yr)	Shortening (mm/yr)	Denudation (mm/yr)	Sources
Southern Alps (NZ)	7000 ± 1000	7.5 ± 0.5	7500 ± 1500	Henderson and Thompson (1999); Herman *et al.* (2010); Norris and Toy (2014)
East Andes	1750 ± 250	6 ± 2	430 ± 290	Safran *et al.* (2005), Champagnac *et al.*, 2012, and references therein
East Cascades	300 ± 100	~0	30 ± 10	Reiners *et al.* (2003)
Middle Europe	1000 ± 500	~0	40 ± 20	Schaller *et al.* (2001); Hoffmann *et al.* (2007)
East Himalayas	3500 ± 2500	17 ± 3	1400 ± 400	Grujic *et al.* (2006), Champagnac *et al.*, 2012, and references therein
East Himalayas	2500 ± 1500	17 ± 3	700 ± 150	Grujic *et al.* (2006), Champagnac *et al.*, 2012 and references therein
West Himalayas	1650 ± 150	15 ± 5	~1800	Bhutiyani (2000); Winiger *et al.* (2005), Champagnac *et al.*, 2012, and references therein
West Himalayas	~600	15 ± 5	280 ± 190	Bhutiyani (2000); Winiger *et al.* (2005), Champagnac *et al.*, 2012, and references therein
Qilian Shan	275 ± 120	5.5 ± 1.8	200 ± 100	Pan *et al.* (2010); Palumbo *et al.* (2011), Champagnac *et al.*, 2012, and references therein
Longshou Shan	~200	5.5 ± 1.8	155 ± 12	Palumbo *et al.* (2010), Champagnac *et al.*, 2012, and references therein
Tian Shan	300 ± 100	10 ± 3	135 ± 140	This study, Métivier and Gaudemer, 1997; Reigber *et al.*, 2001; Sobel *et al.*, 2003, Champagnac *et al.*, 2012, and references herein
Zagros	400 ± 100	8 ± 2	85 ± 75	Ali *et al.* (2003); Javanmard *et al.* (2010), Champagnac *et al.*, 2012, and references therein

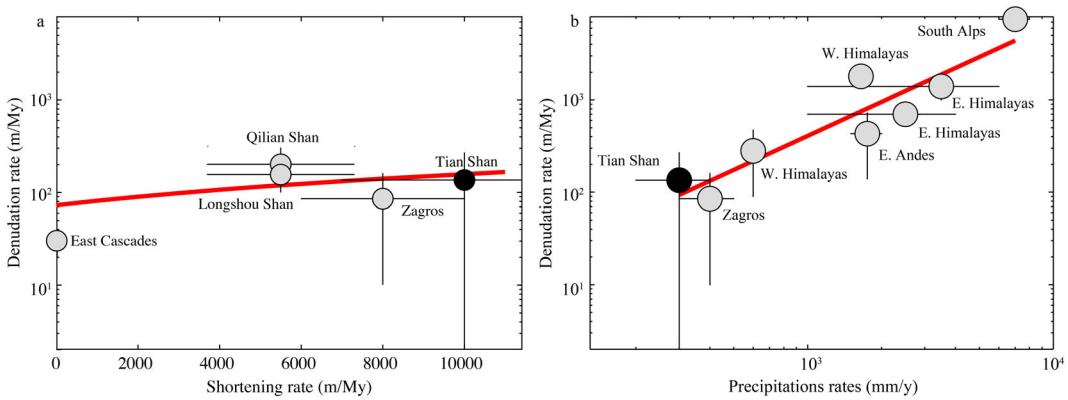

Figure 11. (a) Denudation rates according to shortening rates in mountain ranges where precipitations are close to 300 mm/yr. (b) Denudation rates according to mean annual precipitation in mountain ranges where the shortening rate is close to 1 cm/yr (see Table VI for references). This figure is available in colour online at www.interscience.wiley.com/journal/espl.

deposits of the northern piedmont contain pedogenic carbonates (Charreau *et al.*, 2012; Heilbronn *et al.*, 2015), which form under semi-arid to semi-humid climate with less than 1000 mm/yr of precipitation (Retallack *et al.*, 1997, and references therein). This could imply that the Chinese Tian Shan has been experiencing a low denudation rate for a few tens of millions of years, which is in agreement with geological observations such as preserved Mesozoic surfaces in the mountain range and a limited Cenozoic exhumation (Hendrix *et al.*, 1994; Dumitru *et al.*, 2001; Jolivet *et al.*, 2010). If equilibrium between denudation and rock uplift has been reached, it means that the tectonic uplift rate in the range is also less than a few hundred metres per million years. However, a rough estimate gives a rock uplift rate in the Chinese Tian Shan of 300–700 m/Myr (Avouac and Burov, 1996), which is several times higher than the average denudation rate of the range. It is thus possible that the range has not reached equilibrium. This implies that the response time of this orogenic system in a dry climate is extremely long. Yet, to address this issue fully, the tectonic uplift rate in the Tian Shan remains to be accurately quantified.

Conclusions

Based on mass balances performed on 10 catchment–fan systems, we determine average denudation rates for the northern Chinese Tian Shan of ~100 and ~300 m/Myr for the Middle–Late Pleistocene and Holocene, respectively. The denudation increase between the two periods is climate-driven. It is a direct consequence of the extension of the catchment areas in the piedmont associated with sediment reworking following the last glacial–interglacial transition. However, this evolution did not affect the denudation intensity of the hinterland mountains.

In fact, the average denudation rate in the range did not evolve much between the Middle–Late Pleistocene and Holocene as it varies from ~100 m/Myr to ~170 m/Myr. Accordingly, we propose an average denudation rate in the range of ~135 m/Myr for the last 300 kyr. In agreement with the other studies performed in the same area, the typical denudation rate of the northern Tian Shan is thus of a few hundred metres per million years at maximum, regardless of the space and time scales.

Copyright © 2016 John Wiley & Sons, Ltd.

This is low for such a high and active mountain belt. From a comparison of the denudation rates observed in the Tian Shan and in other ranges, we suggest that, notwithstanding the tectonic activity, a dry climate can dramatically limit the denudation intensity even in orogenic systems with a strong topographic gradient. As a result, the time required to reach equilibrium between denudation and rock uplift could be extremely long in these systems (more than several million years). Therefore, in such climatic contexts, further work on range uplift and topographic evolution should be carried out to constrain better the state of the system in terms of topographic and flux equilibrium.

Appendix A: Construction of the Morpho-sedimentary Maps

The two morpho-sedimentary maps are based on the interpretation of Landsat and DigitalGlobe (in Google Earth) satellite images (28 m and 2.5 m resolution respectively) coupled with the study of the Aster GDEM2 digital elevation model (30 m

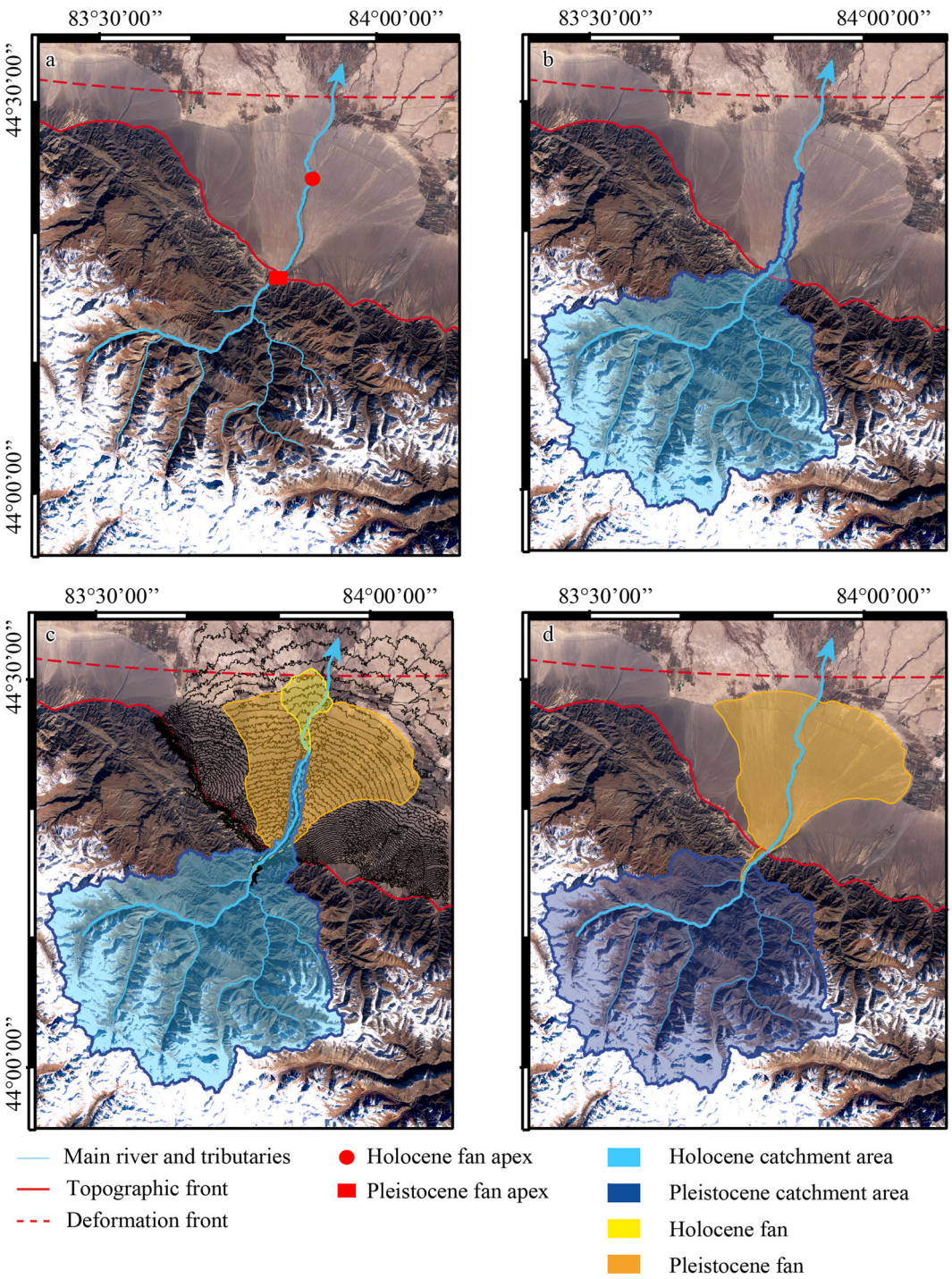

Figure 12. Construction of the morpho-sedimentary maps based on satellite images and DEM analyses: example of the Guertu River system. (a) Localization of the main river and tributaries (blue lines) and of fan apexes (red square and dot). (b) Determination of the Holocene catchment area. (c) Localization of the Holocene (in yellow) and Middle–Late Pleistocene (in orange) fans. (d) Late Pleistocene map inferred from the Holocene one after the suppression of the Holocene fan and catchment area extension. Below the Holocene fan, the Middle–Late Pleistocene fan outlines are interpolated based on the assumption that the fan termination curve is continuous. The topographic (red line) and deformation (red dash-line) fronts are also indicated. This figure is available in colour online at www.interscience.wiley.com/journal/espl.

Copyright © 2016 John Wiley & Sons, Ltd.

horizontal resolution, 7–14 m vertical resolution). The same protocol was used to map the 10 catchment–fan systems for which the position of the F_p fan basal surface can be identified in the field:

1. The path of the main river and its tributaries were identified from the DEM and the satellite images.
2. The positions of the F_p and F_h fan apexes along the main stream were identified (Figure 12a).
3. The Holocene drainage basin was extracted from the DEM, considering the F_h fan apex as the catchment outlet (Figure 12b).
4. The F_p and F_h fan outlines were drawn from the satellite images and from the contour lines extracted from the DEM. The fan toes were considered as the slope break between the fan aprons and the surrounding alluvial plain downstream. The alluvial valley upstream of the fan F_p was also mapped when it contained an important amount of contemporaneous deposits (see also (Jolivet *et al.*, 2014)). At this point, the morpho-sedimentary map of the present-day landscape in the studied area was obtained (Figure 12c; Data S2 and S3).
5. The morpho-sedimentary map of the Late Pleistocene landscape was inferred from the previous one by the suppression of the fan F_h and the Holocene extension of the drainage basin (i.e. the part of the drainage basin located between the F_p and F_h apexes). The F_p fan outlines were interpolated where missing (e.g. where they were covered by Holocene deposits) and the upstream part of the drainage basin was assumed to be the same during the two periods as there is no evidence for a major catchment evolution in the range from the Middle–Late Pleistocene to the Holocene (Figure 12d; Data S4 and S5).

From the two maps, the drainage basin and fan areas, A_d and A_F respectively, were extracted (Tables II and III). The uncertainties $\Delta A_d/A_d$ associated with the drainage basin areas were defined as the overlaps between adjacent catchments and correspond on average to $A_d \pm 0.75\%$ (Tables II and III). Considering that the fan outlines are positioned at the pixel precision, the uncertainties $\Delta A_F/A_F$ on the fan areas were calculated from the Landsat imagery resolution and are, on average, close to $A_F \pm 0.5\%$ (Tables II and III).

Appendix B: Reconstruction of the Volume of Sediments

B.1: Middle–Late Pleistocene fan basal surface

The F_p fan basal surfaces were reconstructed from the fan outlines plotted on the morpho-sedimentary maps and from outcrop observations in the field. During two field campaigns, the main Holocene canyons crossing the piedmont were explored and several places where the basal surface of the fans F_p crops out (Figure 3) were identified. The coordinates and elevation of these basal surface outcrops were then defined.

From a position (x, y, z) known thanks to a GPS, three parameters were measured to determine the coordinates of each basal surface outcrop: Az, the azimuth of the outcrop line-of-sight obtained with a compass; β, the angle between the horizontal and the outcrop line-of-sight given by an inclinometer; and L_1, the distance to the outcrop measured with a distance meter along the line-of-sight. Alternatively, β can be replaced by the measurement of L_0, the horizontal distance to the cliff where the fan base is observed in the Az direction. Coordinates of the basal surface outcrop were then determined by trigonometry (the outcrop KMZ coordinates are given in Supplementary Data S6).

Az, L_0 and L_1 along three rivers (the Kuitun, Jingou and Urumqi rivers), and Az, β and L_1 along the seven others were measured with 18–95 points for each fan basal surface. The two methods lead to similar accuracy and are sensitive to several parameters: the GPS accuracy (7–10 m); the compass and inclinometer accuracy (1∘); and the distance meter maximum capacity (800 m), which is strongly influenced by the atmospheric conditions, in particular by the presence of dust in the air. Therefore, the coordinates of the basal surfaces were determined within 50 m, which is quite satisfying for the longitude and latitude compared to the length of the fans F_p (about 30 km). However, this uncertainty is too high for the outcrop elevations. Consequently, the outcrop elevations were not determined directly from field measurements but extracted from the DEM in coherence with estimations made on outcrops and field pictures.

B.2: Fan and sediment volumes

To obtain the volume of the fans, V_F, the individual volume of the 250×250 m^2 cells of the grids used to model the fan geometry were added up. Consequently, uncertainties on V_F result from the addition of uncertainties on the cell thickness h and the fan area A_F. Uncertainties on h correspond to the difference between the two geometric models (produced with linear or cubic interpolations) and are around 1%. Uncertainties on A_F come from the Landsat resolution and are also around 1%. Another source of uncertainties must be added to consider the reconstruction inconsistencies. In fact, in areas where the fan thickness is small, a coherent geometry could not be modelled from the DEM and the field constraints. Each cell with a thickness of less than 5 m was thus removed from the volume calculation but included in the uncertainties. These cells represent from 1% to 25% of the fan areas (Figure 6e, f). Therefore, the uncertainties $\Delta V_F/V_F$ range from $\pm 3\%$ to 27% (Tables II and III).

To convert V_F into real sediment volumes, $V_{\lambda F}$, the porosity of the deposits was required. As mentioned in the geological setting, all these deposits correspond to conglomerates with grains from silts to metric boulders. From trenches dug in the sediments of the fan F_p and of the present-day river bed of the Urumqi River, a porosity λ of $20 \pm 10\%$ was measured for these conglomerates (Guerit, 2014), in good agreement with published values for such a lithology (Clarke, 1979). The uncertainties on the volumes of sediments, $\Delta V_{\lambda F}/V_{\lambda F}$, result from the addition of the uncertainties on V_F and λ. Therefore, they correspond to:

$$\frac{\Delta V_{\lambda F}}{V_{\lambda F}} = \frac{\Delta V_F}{V_F} + \frac{\Delta \lambda}{\lambda}$$

and range from $\pm 13\%$ to 37% (Tables II and III).

Appendix C: Estimate of the Denudation Rates

The uncertainties associated with the Middle–Late Pleistocene and the total Holocene denudation rates, ϵ_p and ϵ_h, can be calculated as the sum of the uncertainties on the values used to estimate these rates: the volumes of sediments $V_{\lambda F}$; the proportion of the total sediment load trapped in the fans α; the drainage basin areas A_d; and the duration of the fan construction P. Accordingly, the uncertainties associated with

Copyright © 2016 John Wiley & Sons, Ltd.

the Middle–Late Pleistocene denudation rates, $\Delta\epsilon_p/\epsilon_p$, were calculated as follows:

$$\frac{\Delta\epsilon_p}{\epsilon_p} = \frac{\Delta V_{\lambda \mathrm{F}_p}}{V_{\lambda \mathrm{F}_p}} + \frac{\Delta\alpha}{\alpha} + \frac{\Delta A_{dp}}{A_{dp}} + \frac{\Delta P_p}{P_p}$$

and range between 24% and 30% (Table V). Similarly, the uncertainties associated with the total Holocene denudation rates, $\Delta\epsilon_h/\epsilon_h$, were calculated as follows:

$$\frac{\Delta\epsilon_h}{\epsilon_h} = \frac{\Delta V_{\lambda \mathrm{F}_h}}{V_{\lambda \mathrm{F}_h}} + \frac{\Delta\alpha}{\alpha} + \frac{\Delta A_{dh}}{A_{dh}} + \frac{\Delta P_h}{P_h}$$

and are between 33% and 58% (Table V).

The uncertainties associated with the Holocene denudation rates in the piedmont ϵ_c can be calculated as the sum of the uncertainties on the values used to estimate these rates: the volume of sediments reworked from the canyons $V_{\lambda c}$; the areas of the Holocene drainage extensions $A_{d,h-p}$; and the duration of the fan construction P_h. Accordingly, the uncertainties associated with the Holocene denudation rates in the piedmont, $\Delta\epsilon_c/\epsilon_c$, were calculated as follows:

$$\frac{\Delta\epsilon_c}{\epsilon_c} = \frac{\Delta V_{\lambda c}}{V_{\lambda c}} + \frac{\Delta A_{d,h-p}}{A_{d,h-p}} + \frac{\Delta P_h}{P_h}$$

$\Delta A_{d,h-p}/A_{d,h-p}$ being $\Delta A_{dh}/A_{dh} + \Delta A_{dp}/A_{dp}$, and $\Delta V_{\lambda c}/V_{\lambda c}$ being $\Delta V_c/V_c + \Delta\lambda/\lambda$. Consequently, the Holocene denudation rates in the piedmont are associated with uncertainties of 32–82% (Table V).

Finally, the uncertainties associated with the Holocene denudation rates in the range ϵ_r can be calculated as the sum of the uncertainties on the values used to estimate these rates: the difference between the volumes of the sediments trapped in the F_h fans and those reworked from the canyons $V_{\lambda,\mathrm{F}_h-c}$; the proportion of the total sediment load trapped in the fans α; the areas of the Middle–Late Pleistocene drainage basins $A_{d,p}$; and the duration of the fan construction P_h. Accordingly, the uncertainties associated with the Holocene denudation rates in the range, $\Delta\epsilon_r/\epsilon_r$, were calculated as follows:

$$\frac{\Delta\epsilon_r}{\epsilon_r} = \frac{\Delta V_{\lambda,\mathrm{F}_h-c}}{V_{\lambda,\mathrm{F}_h-c}} + \frac{\Delta\alpha}{\alpha} + \frac{\Delta A_{dp}}{A_{dp}} + \frac{\Delta P_h}{P_h}$$

$\Delta V_{\lambda,\mathrm{F}_h-c}/V_{\lambda,\mathrm{F}_h-c}$ being $\Delta V_{\lambda \mathrm{F}_h}/V_{\lambda \mathrm{F}_h} + \Delta V_{\lambda c}/V_{\lambda c}$. The Holocene denudation rates in the range are thus associated with uncertainties of 33–92% (Table V).

Acknowledgements— This work was supported by the French CNRS-INSU and the French–Chinese SALADYN International Associated Laboratory. We thank the ESPL Associate Editors and two anonymous reviewers for their very interesting comments that improved the overall quality of the paper. Acknowledgements are also due to N. Shawwa for his editorial assistance. This paper is the IPGP contribution #3615.

References

Abdrakhmatov KY, Aldazhanov S, Hager B, Hamburger M, Herring T, Kalabaev K, Makarov V, Molnar P, Panasyuk S, Prilepin M, Reilinger R, Sadybakasov I, Souter B, Trapeznikov Y, Tsurkov V, Zubovich A. 1996. Relatively recent construction of the Tien Shan inferred from GPS measurements of present-day crustal deformation rates. *Nature* **384**: 450–453.

Ahnert F. 1970. Functional relationships between denudation, relief, and uplift in large, mid-latitude drainage basins. *American Journal of Science* **268**(3): 243–263.

Ali SA, Rangzan K, Pirasteh S. 2003. Remote sensing and GIS study of tectonics and net erosion rates in the Zagros structural belt, Southwestern Iran. *Mapping Sciences and Remote Sensing* **40**(4): 258–267.

Allen M, Windley B, Zhang C. 1992. Palaeozoic collisional tectonics and magmatism of the Chinese Tien Shan, central Asia. *Tectonophysics* **220**(1): 89–115.

Allen PA, Hovius N. 1998. Sediment supply from landslide-dominated catchments: implications for basin-margin fans. *Basin Research* **10**(1): 19–35.

Avouac JP, Burov EB. 1996. Erosion as a driving mechanism of intracontinental mountain growth. *Journal of Geophysical Research – Solid Earth* **101**(B8): 17747–17769.

Avouac JP, Tapponnier P, Bai M, You H, Wang G. 1993. Active thrusting and folding along the northern Tien Shan and late Cenozoic rotation of the Tarim relative to Dzungaria and Kazakhstan. *Journal of Geophysical Research – Solid Earth* **98**(B4): 6755–6804.

Barnes J, Heins W. 2009. Plio-quaternary sediment budget between thrust belt erosion and foreland deposition in the central Andes, southern Bolivia. *Basin Research* **21**(1): 91–109.

Bhutiyani M. 2000. Sediment load characteristics of a proglacial stream of Siachen Glacier and the erosion rate in Nubra valley in the Karakoram Himalayas, India. *Journal of hydrology* **227**(1): 84–92.

Binnie SA, Phillips WM, Summerfield MA, Fifield LK, Spotila JA. 2010. Tectonic and climatic controls of denudation rates in active orogens: the San Bernardino Mountains, California. *Geomorphology* **118**(3): 249–261.

Brown ET, Stallard RF, Larsen MC, Raisbeck GM, Yiou F. 1995. Denudation rates determined from the accumulation of in situ-produced ^{10}Be in the Luquillo Experimental Forest, Puerto Rico. *Earth and Planetary Science Letters* **129**(1): 193–202.

Bullen M, Burbank D, Garver J. 2003. Building the northern Tien Shan: integrated thermal, structural, and topographic constraints. *Journal of Geology* **111**(2): 149–165.

Burbank D, Blythe A, Putkonen J, Pratt-Sitaula B, Gabet E, Oskin M, Barros A, Ojha T. 2003. Decoupling of erosion and precipitation in the Himalayas. *Nature* **426**(6967): 652–655.

Burchfiel BC, Brown ET, Qidong D, Xianyue F, Jun L, Molnar P, Jianbang S, Zhangming W, Huichuan Y. 1999. Crustal shortening on the margins of the Tien Shan, Xinjiang, China. *International Geology Review* **41**(8): 665–700.

Burtman VS, Skobelev SF, Molnar P. 1996. Late Cenozoic slip on the talas–ferGhana fault, the Tien Shan, central Asia. *Geological Society of America Bulletin* **108**(8): 1004–1021.

Calvès G, Toucanne S, Jouet G, Charrier S, Thereau E, Etoubleau J, Marsset T, Droz L, Bez M, Jorry S, Mulder T, Lericolais G. 2013. Inferring denudation variations from the sediment record; an example of the last glacial cycle record of the Golo Basin and watershed, East Corsica, western Mediterranean sea. *Basin Research* **25**: 197–218.

Carretier S, Regard V, Vassallo R, Aguilar G, Martinod J, Riquelme R, Pepin E, Charrier R, Hérail G, Farías M, Guyot JL, Vargas G, Lagane C. 2013. Slope and climate variability control of erosion in the Andes of central Chile. *Geology* **41**(2): 195–198.

Carretier S, Regard V, Vassallo R, Martinod J, Christophoul F, Gayer E, Audin L, Lagane C. 2015. A note on ^{10}Be-derived mean erosion rates in catchments with heterogeneous lithology: examples from the western Central Andes. *Earth Surface Processes and Landforms* **40**(13): 1719–1729.

Champagnac JD, Molnar P, Sue C, Herman F. 2012. Tectonics, climate, and mountain topography. *Journal of Geophysical Research* **117**: B02403.

Chappell J, Zheng H, Fifield K. 2006. Yangtse River sediments and erosion rates from source to sink traced with cosmogenic ^{10}be: sediments from major rivers. palaeogeography, Palaeoclimatology. *Palaeoecology* **241**(1): 79–94.

Charreau J, Chen Y, Gilder S, Barrier L, Dominguez S, Augier R, Sen S, Avouac JP, Gallaud A, Graveleau F, Wang Q. 2009a. Neogene uplift of the Tian Shan Mountains observed in the magnetic record of the Jingou River section (northwest China). *Tectonics* **28**(2): TC2008.

Charreau J, Gumiaux C, Avouac JP, Augier R, Chen Y, Barrier L, Gilder S, Dominguez S, Charles N, Wang Q. 2009b. The Neogene Xiyu Formation, a diachronous prograding gravel wedge at front of the

Copyright © 2016 John Wiley & Sons, Ltd.

Tianshan: climatic and tectonic implications. *Earth and Planetary Science Letters* **287**: 298–310.

Charreau J, Blard PH, Puchol N, Avouac JP, Lallier-Verges E, Bourles D, Braucher R, Gallaud A, Finkel R, Jolivet M, Chen Y, Roy P. 2011. Paleo-erosion rates in Central Asia since 9 Ma: a transient increase at the onset of Quaternary glaciations? *Earth and Planetary Science Letters* **304**(1–2): 85–92.

Charreau J, Kent-Corson ML, Barrier L, Augier R, Ritts BD, Chen Y, France-Lanord C, Guilmette C. 2012. A high-resolution stable isotopic record from the Junggar Basin (NW China): implications for the paleotopographic evolution of the Tianshan Mountains. *Earth and Planetary Science Letters* **341**: 158–169.

Chen K, Gumiaux C, Augier R, Martelet G, Chen Y, Wang Q. 2014. Integrated multidisciplinary approach to constrain range fronts structure, a case study of the northern Tianshan piedmont (NW China). *Bulletin de la Société Géologique de France* **185**(6): 379–392.

Church M, Ryder JM. 1972. Paraglacial sedimentation: a consideration of fluvial processes conditioned by glaciation. *Geological Society of America Bulletin* **83**(10): 3059–3072.

Church M, Slaymaker O. 1989. Disequilibrium of Holocene sediment yield in glaciated British Columbia. *Nature* **337**(6206): 452–454.

Clarke RH. 1979. Reservoir properties of conglomerates and conglomeratic sandstones. *American Association of Petroleum Geologists Bulletin* **63**(5): 799–809.

Clift PD. 2006. Controls on the erosion of Cenozoic Asia and the flux of clastic sediment to the ocean. *Earth and Planetary Science Letters* **241**(3): 571–580.

Clift PD, Giosan L, Blusztajn J, Campbell I, Allen C, Pringle M, Tabrez A, Danish M, Rabbani M, Alizai A, Carter A, Lueckge A. 2008. Holocene erosion of the Lesser Himalaya triggered by intensified summer monsoon. *Geology* **36**(1): 79–82.

Covault JA, Craddock WH, Romans BW, Fildani A, Gosai M. 2013. Spatial and temporal variations in landscape evolution: historic and longer-term sediment flux through global catchments. *Journal of Geology* **121**: 35–56.

Dadson S, Hovius N, Chen H, Dade W, Hsieh M, Willett S, Hu J, Horng M, Chen M, Stark C, Lague D, Lin J. 2003. Links between erosion, runoff variability and seismicity in the Taiwan orogen. *Nature* **426**(6967): 648–651.

de Vente J, Poesen J, Arabkhedri M, Verstraeten G. 2007. The sediment delivery problem revisited. *Progress in Physical Geography* **31**(2): 155–178.

Delmas M, Braucher R, Gunnell Y, Guillou V, Calvet M, Bourlès D, and ASTER Team. 2015. Constraints on Pleistocene glaciofluvial terrace age and related soil chronosequence features from vertical ^{10}Be profiles in the ariège River catchment (pyrenees, France). *Global Planet Change* **132**: 39–53.

Dumitru TA, Zhou D, Chang EZ, Graham SA, Hendrix MS, Sobel ER, Carroll AR. 2001. Uplift, exhumation, and deformation in the Chinese Tian Shan. *Memoirs – Geological Society of America* **194**: 71–100.

Ehlers TA, Farley KA. 2003. Apatite (u–th)/he thermochronometry: methods and applications to problems in tectonic and surface processes. *Earth and Planetary Science Letters* **206**(1): 1–14.

Farías M, Charrier R, Carretier S, Martinod J, Fock A, Campbell D, Cáceres J, Comte D. 2008. Late Miocene high and rapid surface uplift and its erosional response in the Andes of central Chile (33∘–35∘ S). *Tectonics* **27**(1): TC1005.

Gabet EJ, Burbank DW, Pratt-Sitaula B, Putkonen J, Bookhagen B. 2008. Modern erosion rates in the High Himalayas of Nepal. *Earth and Planetary Science Letters* **267**(3): 482–494.

Gallaud A. 2008. *Interaction Orogenèse – Climat – Erosion en Asie Centrale durant le Cénozoïque : l'impact de la surrection de la chaine du Tianshan sur le climat dans le bassin du Junggar*, University Orléans, France.

Galy A, France-Lanord C. 2001. Higher erosion rates in the Himalaya: geochemical constraints on riverine fluxes. *Geology* **29**(1): 23–26.

Gao J, Li M, Xiao X, Tang Y, He G. 1998. Paleozoic tectonic evolution of the Tianshan Orogen, northwestern China. *Tectonophysics* **287**(1–4): 213–231.

Gong Z, Li SH, Li B. 2014. The evolution of a terrace sequence along the Manas River in the northern foreland basin of Tian Shan, China, as inferred from optical dating. *Geomorphology* **213**: 201–212.

Granger DE, Kirchner JW, Finkel R. 1996. Spatially averaged long-term erosion rates measured from in situ-produced cosmogenic nuclides in alluvial sediment. *Journal of Geology* **104**: 249–257.

Graveleau F. 2008. *Interactions Tectonique, Erosion, Sédimentation dans les avant-pays de chaînes : modélisation analogique et étude des piémonts de l'est du Tian Shan (Asie centrale)*, Université Montpellier II Sciences et Techniques du Languedoc, France.

Grujic D, Coutand I, Bookhagen B, Bonnet S, Blythe A, Duncan C. 2006. Climatic forcing of erosion, landscape, and tectonics in the Bhutan Himalayas. *Geology* **34**(10): 801–804.

Guan S, Li B, He D, Shaw JH, Chen Z. 2009. Recognition and exploration of structural wedges: a case study in the southern margin of Junggar Basin, China. *Earth Science Frontiers* **16**(3): 129–137.

Guerit L. 2014. *Caractéristiques morpho-sédimentaires des cônes alluviaux et reconstitution de leurs paléo-flux d'eau et de sédiments: exemples naturels du piedmont nord du Tian Shan (Xinjiang, Chine) et modélisation expérimentale*, Institut de Physique du Globe de Paris, Université Paris Diderot, France.

Heilbronn G, Boulvais P, Marchand E, Robin C, Bourquin S, Barrier L, Jia Y, Fu B. 2015. Stable isotope characterization of pedogenic and lacustrine carbonates from the Chinese Tian Shan: constraints on the Mesozoic–Lower Cenozoic paleo-environmental evolution. *Chemie der Erde-Geochemistry* **75**(1): 133–141.

Henderson R, Thompson S. 1999. Extreme rainfalls in the Southern Alps of New Zealand. *Journal of Hydrology (NZ)* **38**(2): 309–330.

Hendrix M, Graham S, Carroll A, Sobel E, McKnight C, Schulein B, Wang Z. 1992. Sedimentary record and climatic implications of recurrent deformation un the Tian Shan: evidence from mesozoic strata of the north Tarim, south Junggar, and Turpan basins, northwest China. *Geological society of America Bulletin* **104**(1): 53–79.

Hendrix MS, Dumitru TA, Graham SA. 1994. Late Oligocene–early Miocene unroofing in the Chinese Tian Shan: an early effect of the India–asia collision. *Geology* **22**(6): 487–490.

Herman F, Rhodes E, Braun J, Heiniger L. 2010. Uniform erosion rates and relief amplitude during glacial cycles in the Southern Alps of New zealand, as revealed from OSL–thermochronology. *Earth and Planetary Science Letters* **297**: 183–189.

Hinderer M. 2012. From gullies to mountain belts: a review of sediment budgets at various scales. *Sedimentary Geology* **280**: 21–59.

Hippe K, Kober F, Zeilinger G, Ivy-Ochs S, Maden C, Wacker L, Kubik PW, Wieler R. 2012. Quantifying denudation rates and sediment storage on the eastern Altiplano, Bolivia, using cosmogenic ^{10}Be, ^{26}Al, and in situ ^{14}C. *Geomorphology* **179**: 58–70.

Hoffmann T, Erkens G, Cohen KM, Houben P, Seidel J, Dikau R. 2007. Holocene floodplain sediment storage and hillslope erosion within the Rhine catchment. *The Holocene* **17**(1): 105–118.

Hornung J, Pflanz D, Hechler A, Beer A, Hinderer M, Maisch M, Bieg U. 2010. 3-D architecture, depositional patterns and climate triggered sediment fluxes of an alpine alluvial fan (Samedan, Switzerland). *Geomorphology* **115**: 202–214.

Hovius N. 1998. Controls on sediment supply by large rivers. *Special Publications of SEPM* **59**: 3–16.

Iaffaldano G, Husson L, Bunge HP. 2011. Monsoon speeds up Indian plate motion. *Earth and Planetary Science Letters* **304**(3): 503–510.

Insel N, Ehlers TA, Schaller M, Barnes JB, Tawackoli S, Poulsen CJ. 2010. Spatial and temporal variability in denudation across the Bolivian Andes from multiple geochronometers. *Geomorphology* **122**(1): 65–77.

Javanmard S, Yatagai A, Nodzu M, BodaghJamali J, Kawamoto H. 2010. Comparing high-resolution gridded precipitation data with satellite rainfall estimates of TRMM 3B42 over Iran. *Advances in Geosciences* **25**: 119–125.

Jayko AS. 2005. Late Quaternary denudation, Death and Panamint valleys, eastern California. *Earth-Science Reviews* **73**(1): 271–289.

Jolivet M, Ritz JF, Vassallo R, Larroque C, Braucher R, Todbileg M, Chauvet A, Sue C, Arnaud N, De Vicente R, Arzhanikova A, Arzhanikov S. 2007. The Mongolian summits: an uplifted, flat, old but still preserved erosion surface. *Geology* **35**(10): 871–874.

Copyright © 2016 John Wiley & Sons, Ltd.

Jolivet M, Dominguez S, Charreau J, Chen Y, Li Y, Wang Q. 2010. Mesozoic and Cenozoic tectonic history of the central Chinese Tian Shan: reactivated tectonic structures and active deformation. *Tectonics* **29**: TC6019.

Jolivet M, Arzhannikov S, Arzhannikova A, Chauvet A, Vassallo R, Braucher R. 2013a. Geomorphic Mesozoic and Cenozoic evolution in the Oka-Jombolok region (east sayan ranges, siberia). *Journal of Asian Earth Sciences* **62**: 117–133.

Jolivet M, Heilbronn G, Robin C, Barrier L, Bourquin S, Guo Z, Jia Y, Guerit L, Yang W, Fu B. 2013b. Reconstructing the Late Palaeozoic–Mesozoic topographic evolution of the Chinese Tian Shan: available data and remaining uncertainties. *Advances en Geosciences* **1**: 1–12.

Jolivet M, Barrier L, Dominguez S, Guerit L, Heilbronn G, Fu B. 2014. Unbalanced sediment budgets in the catchment–alluvial fan system of the Kuitun River (northern Tian Shan, China): implications for the erosion and uplift rate estimates in mountain ranges. *Geomorphology* **214**: 168–182.

Kiefer E, Dorr MJ, Ibbeken H, Gotze HJ. 1997. Gravity-based mass balance of an alluvial fan giant: the Arcas Fan, Pampa del Tamarugal, Northern Chile. *Andean Geology* **24**(2): 165–185.

Kirchner J, Finkel R, Riebe C, Granger D, Clayton J, King J, Megahan W. 2001. Mountain erosion over 10 yr, 10 k.y., and 10 m.y. time scales. *Geology* **29**(7): 591–594.

Kober F, Ivy-Ochs S, Schlunegger F, Baur H, Kubik PW, Wieler R. 2007. Denudation rates and a topography-driven rainfall threshold in northern Chile: multiple cosmogenic nuclide data and sediment yield budgets. *Geomorphology* **83**: 97–120.

Kong P, Na C, Fink D, Ding L, Huang F. 2007. Erosion in northwest Tibet from in-situ-produced cosmogenic ^{10}Be and ^{26}Al in bedrock. *Earth Surface Processes and Landforms* **32**(1): 116–125.

Lal D, Harris NB, Sharma KK, Gu Z, Ding L, Liu T, Dong W, Caffee MW, Jull A. 2004. Erosion history of the Tibetan Plateau since the last interglacial: constraints from the first studies of cosmogenic ^{10}Be from Tibetan bedrock. *Earth and Planetary Science Letters* **217**(1): 33–42.

Lane EW, Borland WM. 1951. Estimating bed load. *Transactions - American Geophysical Union* **32**: 121–123.

Li Y, Liu G, Cui Z. 2001. Glacial valley cross-profile morphology, Tian Shan Mountains, China. *Geomorphology* **38**(1): 153–166.

Liu Y, Métivier F, Gaillardet J, Ye B, Meunier P, Narteau C, Lajeunesse E, Han T, Malverti L. 2011. Erosion rates deduced from seasonal mass balance along the upper Urumqi River in Tianshan. *Solid Earth* **2**: 283–301.

Lu H, Burbank DW, Li Y. 2010. Alluvial sequence in the north piedmont of the Chinese Tian Shan over the past 550 kyr and its relationship to climate change. *Palaeogeogr Palaeoclimatol Palaeoecol* **285**(3–4): 343–353.

Matmon A, Bierman P, Larsen J, Southworth S, Pavich M, Caffee M. 2003. Temporally and spatially uniform rates of erosion in the southern Appalachian Great Smoky Mountains. *Geology* **31**(2): 155–158.

Matmon A, Simhai O, Amit R, Haviv I, Porat N, McDonald E, Benedetti L, Finkel R. 2009. Desert pavement-coated surfaces in extreme deserts present the longest-lived landforms on Earth. *Geological Society of America Bulletin* **121**(5–6): 688–697.

Métivier F, Gaudemer Y. 1997. Mass transfer between eastern Tien Shan and adjacent basins (central asia): Constraints on regional tectonics and topography. *Geophysical Journal International* **128**(1): 1–17.

Metivier F, Gaudemer Y. 1999. Stability of output fluxes of large rivers in South and East Asia during the last 2 million years: implications on floodplain processes. *Basin Research* **11**(4): 293–303.

Métivier F, Gaudemer Y, Tapponnier P, Klein M. 1999. Mass accumulation rates in Asia during the Cenozoic. *Geophysical Journal International* **137**(2): 280–318.

Meunier P, Métivier F, Lajeunesse E, Mériaux A, Faure J. 2006. Flow pattern and sediment transport in a braided river: the 'torrent de St Pierre' (french alps). *Journal of Hydrology* **330**(3): 496–505.

Molnar P, England P. 1990. Late Cenozoic uplift of mountain ranges and global climate change: chicken or egg? *Nature* **346**: 29–34.

Molnar PP, Brown ET, Burchfiel BC, Qidong D, Xianyue F, Jun L, Raisbeck GM, Jianbang S, Zhangming W, Yiou F, Huichuan Y. 1994. Quaternary climate change and the formation of river terraces across growing anticlines on the north flank of the Tien Shan, China. *Journal of Geology* **102**(5): 583–602.

Montgomery DR, Brandon MT. 2002. Topographic controls on erosion rates in tectonically active mountain ranges. *Earth and Planetary Science Letters* **201**(3–4): 481–489.

Norris RJ, Toy VG. 2014. Continental transforms: a view from the Alpine Fault. *Journal of Structural Geology* **64**: 3–31.

Norton KP, von Blanckenburg F, DiBiase R, Schlunegger F, Kubik PW. 2011. Cosmogenic ^{10}Be-derived denudation rates of the Eastern and Southern European Alps. *International Journal of Earth Sciences* **100**(5): 1163–1179.

Oguchi T. 1997. Late quaternary sediment budget in alluvial-fan-source-basin systems in Japan. *Journal of Quaternary* **12**(5): 381–390.

Palumbo L, Hetzel R, Tao M, Li X. 2010. Topographic and lithologic control on catchment-wide denudation rates derived from cosmogenic 10 Be in two mountain ranges at the margin of NE Tibet. *Geomorphology* **117**(1): 130–142.

Palumbo L, Hetzel R, Tao M, Li X. 2011. Catchment-wide denudation rates at the margin of NE Tibet from in situ-produced cosmogenic ^{10}Be. *Terra Nova* **23**(1): 42–48.

Pan B, Geng H, Hu X, Sun R, Wang C. 2010. The topographic controls on the decadal-scale erosion rates in Qilian Shan Mountains, NW China. *Earth and Planetary Science Letters* **292**(1–2): 148–157.

Poisson B. 2002. *Impact du climat et de la tectonique sur l'évolution géomorphologique d'un piedmont: exemple du piémont Nord du Tian Shan depuis la fin du Pléistocène*, Université Paris XI, France.

Poisson B, Avouac J. 2004. Holocene hydrological changes inferred from alluvial stream entrenchment in North Tian Shan (northwestern China). *Journal of Geology* **112**(2): 231–249.

Puchol N. 2013. *Détermination des paléo-taux d'érosion par l'utilisation des isotopes cosmogéniques. Cas de la transition Pliocène–Pléistocène*, Université de Lorraine, France.

Raymo M, Ruddiman WF. 1992. Tectonic forcing of late Cenozoic climate. *Nature* **359**(6391): 117–122.

Reigber C, Michel G, Galas R, Angermann D, Klotz J, Chen J, Papschev A, Arslanov R, Tzurkov V, Ishanov M. 2001. New space geodetic constraints on the distribution of deformation in Central Asia. *Earth and Planetary Science Letters* **191**(1): 157–165.

Reiners PW, Ehlers TA, Mitchell SG, Montgomery DR. 2003. Coupled spatial variations in precipitation and long-term erosion rates across the Washington Cascades. *Nature* **426**(6967): 645–647.

Retallack GJ. 1997. *Colour Guide to Paleosols*. Wiley: Chichester.

Rhodes T, Gasse F, Lin R, Fontes J, Wei K, Bertrand P, Gibert E, Melieres F, Tucholka P, Wang Z, Cheng Z. 1996. A late Pleistocene–Holocene lacustrine record from Lake Manas, Zunggar (northern Xinjiang, western China). palaeogeography, Palaeoclimatology. *Palaeoecology* **120**(1–2): 105–121.

Riebe C, Kirchner J, Granger D, Finkel R. 2001. Strong tectonic and weak climatic control of long-term chemical weathering rates. *Geology* **29**(6): 511–514.

Safran EB, Bierman PR, Aalto R, Dunne T, Whipple KX, Caffee M. 2005. Erosion rates driven by channel network incision in the Bolivian Andes. *Earth Surface Processes and Landforms* **30**(8): 1007–1024.

Schaller M, von Blanckenburg F, Hovius N, Kubik P. 2001. Large-scale erosion rates from in situ-produced cosmogenic nuclides in European river sediments. *Earth and Planetary Science Letters* **188**(3–4): 441–458.

Schiefer E, Hassan MA, Menounos B, Pelpola CP, Slaymaker O. 2010. Interdecadal patterns of total sediment yield from a montane catchment, southern Coast Mountains, British Columbia, Canada. *Geomorphology* **118**(1–2): 207–212.

Simoes M, Braun J, Bonnet S. 2010. Continental-scale erosion and transport laws: a new approach to quantitatively investigate macroscale landscapes and associated sediment fluxes over the geological past. geochemistry, Geophysics. *Geosystems* **11**(9): Q09001.

Sobel ER, Hilley GE, Strecker MR. 2003. Formation of internally drained contractional basins by aridity-limited bedrock incision. *Journal of Geophysical Research: Solid Earth (1978–2012)* **108**(B7): 2344.

Copyright © 2016 John Wiley & Sons, Ltd.

Summerfield M, Hulton N. 1994. Natural controls of fluvial denudation rates in major world drainage basins. *Journal of Geophysical Research: Solid Earth (1978–2012)* **99**(B7): 13871–13883.

Sun J, Zhang Z. 2008. Palynological evidence for the mid-Miocene climatic optimum recorded in Cenozoic sediments of the Tian Shan Range, northwestern China. *Global Planet Change* **64**(1): 53–68.

Tapponnier P, Molnar P. 1977. Active faulting and tectonics in China. *Journal of Geophysical Research* **82**(20): 2905–2930.

Torres Acosta V, Schildgen TF, Clarke BA, Scherler D, Bookhagen B, Wittmann H, von Blanckenburg F, Strecker MR. 2015. Effect of vegetation cover on millennial-scale landscape denudation rates in East Africa. *Lithosphere* **L402**: 1.

Vance D, Bickle M, Ivy-Ochs S, Kubik P. 2003. Erosion and exhumation in the Himalaya from cosmogenic isotope inventories of river sediments. *Earth and Planetary Science Letters* **206**(3–4): 273–288.

von Blanckenburg F. 2005. The control mechanisms of erosion and weathering at basin scale from cosmogenic nuclides in river sediment. *Earth and Planetary Science Letters* **237**(3): 462–479.

Whipple KX. 2009. The influence of climate on the tectonic evolution of mountain belts. *Nature Geoscience* **2**(2): 97–104.

Windley BF, Allen MB, Zhang C, Zhao ZY, Wang GR. 1990. Paleozoic accretion and Cenozoic redeformation of the Chinese Tien Shan range, central Asia. *Geology* **18**(2): 128–131.

Winiger M, Gumpert M, Yamout H. 2005. Karakorum–hindukush–western Himalaya: assessing high-altitude water resources. *Hydrological Processes* **19**(12): 2329–2338.

Wittmann H, von Blanckenburg F, Kruesmann T, Norton KP, Kubik PW. 2007. Relation between rock uplift and denudation from cosmogenic nuclides in river sediment in the Central Alps of Switzerland. *Journal of Geophysical Research: Earth Surface* **112**: F04010.

Xu X, Kleidon A, Miller L, Wang S, Wang L, Dong G. 2010. Late Quaternary glaciation in the Tianshan and implications for palaeoclimatic change: a review. *Boreas* **39**(2): 215–232.

Yang X, Li A, Hunag W. 2013. Uplift differential of active fold zones during the late Quaternary, northern piedmonts of the Tianshan Mountains, China. *Science China Earth Sciences* **56**(5): 794–805.

Yi C, Liu K, Cui Z, Jiao K, Yao T, He Y. 2004. AMS Radiocarbon dating of late Quaternary glacial landforms, source of the Urumqi River, Tien Shan: a pilot study of ^{14}C dating on inorganic carbon. *Quaternary International* **121**(1): 99–107.

Zhang P, Molnar P, Downs W. 2001. Increased sedimentation rates and grain sizes 2–4 Myr ago due to the influence of climate change on erosion rates. *Nature* **410**(6831): 891–897.

Zhao J, Liu S, He Y, Song Y. 2009. Quaternary glacial chronology of the Ateaoyinake River Valley, Tianshan Mountains, China. *Geomorphology* **103**: 276–284.

Zhou D, Graham SA, Chang EZ, Wang B, Hacker B. 2001. Paleozoic tectonic amalgamation of the Chinese Tian Shan: evidence from a transect along the Dushanzi-Kuqa Highway. *Memoirs – Geological Society of America* **194**: 23–46.

Zhou L, Yang F, Shao X. 1999. *River Hydrology and Water Resources in Xinjiang, Urumqi (in Chinese)*. Xinjiang Science and Technology Press: Xinjiang, China.

Zhou SZ, Jiao KQ, Zhao JD, Zhang SQ, Cui JX, Xu LB. 2002. Geomorphology of the Urumqi River Valley and the uplift of the Tianshan Mountains in Quaternary. *Science China Series D : Earth Sciences* **45**(11): 961–968.

Zubovich AV, Wang Xq, Scherba YG, Schelochkov GG, Reilinger R, Reigber C, Mosienko OI, Molnar P, Michajljow W, Makarov VI, Li J, Kuzikov S, Herring T, Hamburger M, Bradford H, Dang Y, Bragin V, Beisenbaev R. 2010. GPS velocity field for the Tien Shan and surrounding regions. *Tectonics* **29**(6): TC6014.

Supporting Information

Supporting information may be found in the online version of this article at the publisher's web site.

Copyright © 2016 John Wiley & Sons, Ltd.